NPL
National Physical Laboratory

Report

NPL REPORT

DEPC-MPR-043

Prediction of the Impact Performance of Plastics Mouldings

G D Dean and L E Crocker

NOT RESTRICTED

February 2006

dti
National Measurement System

National Physical Laboratory | Hampton Road | Teddington | Middlesex | United Kingdom | TW11 0LW

Switchboard 020 8977 3222 | **NPL Helpline** 020 8943 6880 | **Fax** 020 8943 6458 | **www.npl.co.uk**

dti

The DTI drives our ambition of 'prosperity for all' by working to create the best environment for business success in the UK. We help people and companies become more productive by promoting enterprise, innovation and creativity.

We champion UK business at home and abroad. We invest heavily in world-class science and technology. We protect the rights of working people and consumers. And we stand up for fair and open markets in the UK, Europe and the world.

The National Physical Laboratory is operated on behalf of the DTI by NPL Management Limited, a wholly owned subsidiary of Serco Group plc

Prediction of the Impact Performance of Plastics Mouldings

G D Dean and L E Crocker

Division of Engineering and Process Control,
National Physical Laboratory

ABSTRACT

Measurements have been made of true stress vs true strain curves under tension, compression and shear on a rubber-toughened, propylene-ethylene copolymer used for the manufacture of motor vehicle interior door trim. Results are analysed to determine the properties and parameters required by selected elastic-plastic models for the simulation of impact performance using finite element methods. For this purpose, measurements are required out to large strains and over a wide range of strain rate, which includes very high rates (~ 1000 s^{-1}) associated with impact events. The determination of properties at high strain rates is achieved by modelling measurements at low and moderate strain rates and calculating the behaviour at high strain rates by extrapolation. Measurements of stress/strain curves under tension, shear and compression and of Poisson's ratio with strain are used to derive parameters for the von Mises and linear Drucker-Prager models and for a new model that takes account of the influence of cavitation on plastic deformation. Limitations in the applicability of the first two models for describing the deformation behaviour of the copolymer are demonstrated.

Finite element analysis (FEA) is used to predict the deformation of subcomponents cut from interior door trim mouldings supplied by Jaguar Land Rover. Predictions are compared with measurements at a range of loading speeds. The FE simulation has been analysed by using different element types (solid/shell), different analysis types (rate-independent/rate-dependent) and studying the influence of friction and impact location. Results are presented of a small study carried out to indicate how sensitive the predictions are to changes in the cavitation model parameters.

ISSN 1744-0270

National Physical Laboratory
Hampton Road, Teddington, Middlesex, TW11 0LW

Approved on behalf of the Managing Director, NPL,
by Dr M G Cain, Knowledge Leader, Process Materials Team
authorised by Director, Engineering and Process Control Division

CONTENTS

1 INTRODUCTION

Tough plastics have characteristic properties that make them particularly suited to applications where accidental impact loading is possible, and the material must withstand this without failure or must limit the force level sustained by other objects in the impact event. These applications include housings for domestic and electronic appliances, structural packaging and personal protection equipment. In particular, plastics are used for many components in motor vehicles that may be impacted by passengers or pedestrians in a road accident. Ideally, these components should minimise damage to the human body part involved in the impact. The ability to confidently predict the response of a plastics product under impact loading is therefore an important aspect of the design of these products in order to optimise safety and reliability in their performance. Finite element analysis enables the optimisation of component design without lengthy experimental test schedules as the influence of factors such as geometry; loading, etc. can be rapidly and easily explored.

A finite element analysis can be used to predict performance under impact, but as with many predictive methods, the accuracy of results is uncertain. The main reasons for this uncertainty in the case of plastics materials are related to the use of a suitable materials model for describing the deformation behaviour of the material and the acquisition of property data, required by the model, of adequate accuracy. Elastic-plastic models are used in finite element systems to describe large strain, non-linear behaviour when this is caused by yielding and flow. These models employ a yield criterion and a flow law to calculate components of stress and strain under conditions where the deformation behaviour is non-linear. The elastic-plastic models generally available in finite element systems were developed for metals and some other materials, and their validity for a wide range of plastics is uncertain. In particular, there is an important class of plastics that undergo cavitation in microscopic regions of the polymer under stress states and stress levels where there is a dilatational component of stress that is sufficient to nucleate the cavities. Cavitation is usually visible as stress whitening and is responsible for increased toughness by promoting localised shear yielding in the material between cavities [1]. It will therefore lower the yield stress under those stress states for which the hydrostatic stress component is sufficient to cause cavitation.

In rubber-toughened plastics, the rubber particles have been introduced to improve toughness and are sites for cavity nucleation. In semi-crystalline polymers where the amorphous phase is rubbery, such as polyethylenes and polypropylenes at ambient temperatures, the sites of cavitation are the amorphous regions between crystallites. The material studied here is a rubber-toughened, propylene-ethylene copolymer. The presence of ethylene groups copolymerised with propylene groups makes the amorphous regions more mobile and therefore more amenable to the nucleation of cavities. The presence of rubber particles provides more sites for cavity formation.

Elastic-plastic models currently available in finite element systems are unable to accurately describe the non-linear deformation behaviour of these materials under a wide range of stress states [2, 3]. A new elastic-plastic model is described in this report that takes account of the influence of cavitation on yielding and plastic flow. The determination of properties and parameters for the cavitation model requires measurements of stress/strain behaviour on test specimens under different stress states. Tests under uniaxial tension, shear and uniaxial compression are used for the analyses in this report. These measurements have also been used to derive parameters for other elastic-plastic models that are available in finite element systems. By using all the measured data, limitations in these more simple models for describing the deformation behaviour of the types of polymer studied here are demonstrated.

To maximise accuracy in predictions, it is necessary to take account of the dependence of properties on strain rate. Measurements of stress/strain curves at the high strain rates associated with impact events are difficult because of the high test speeds and are subject to errors arising from problems with the measurement of strain and from resonance and transient vibrations in the force transducer, test specimen and test assembly. A procedure is described in this part for deriving hardening curves at high strain rates by modelling measurements made at low and moderate rates, where measurement accuracy is good, and calculating curves at higher strain rates by extrapolation.

In this report, the accuracies that can be achieved with the elastic-plastic models are explored through predictions and measurements of the deformation behaviour of two

subcomponents obtained by cutting regions from interior door trim panels for a Land Rover motor vehicle. The design of these panels is a major concern for Land Rover in order to offer maximum protection to passengers in the event of a side impact. These subcomponents are small, non-planar regions (approximately 200 mm × 200 mm) of a door panel whose geometries are relatively simple compared with the geometry of the whole panel. Clamping devices have been manufactured so that the subcomponents can be supported in a universal test machine and loaded by a hemispherical surface. Predictions of deformation are compared with measurements made over a range of loading speeds. The ease with which different loading conditions can be simulated within FEA has been illustrated. A series of analyses has been run to study the effect of impact location, and to cover the possibility of experimental variability by looking at slightly different loading angles.

There are many decisions to be made when setting up an FE model, such as element type, material model selection and analysis type. The FE simulation itself has been analysed by using different element types (solid and shell), different analysis types (rate-dependent, rate-independent) and studying the influence of friction. For reliable predictions, accurate materials parameters must be used. This has been the focus of sensitivity analyses, which have been carried out to indicate how sensitive predictions are to changes in the cavitation model parameters.

2 ELASTIC-PLASTIC MODELS

2.1 GENERAL

Elastic-plastic models are used by finite element methods to describe large strain, non-linear behaviour when this is caused by yielding and flow. With these models, behaviour at low strains is taken to be linear elastic and characterised by two materials parameters which are commonly the Young's modulus E and the elastic Poisson's ration ν^e. The onset of non-linearity in a stress/strain curve is attributed to plastic deformation and occurs at a stress level regarded as the first yield stress. The subsequent increase in stress with strain is associated with the effects of strain hardening. In this non-linear region, the total strain ε is considered to be the sum of an elastic component ε^e and a plastic component ε^p so that

$$\varepsilon = \varepsilon^e + \varepsilon^p \tag{1}$$

Plastic strain hardening is then characterised by a curve (hardening curve) describing the variation of yield stress with plastic strain. In the case of tensile hardening, equation (1) gives the tensile component of plastic strain ε_T^p at the tensile stress σ_T as

$$\varepsilon_T^p = \varepsilon_T - \frac{\sigma_T}{E} \tag{2}$$

where ε_T is the total tensile strain. The tensile hardening curve is then the function $\sigma_T\left(\varepsilon_T^p\right)$.

Stress analysis calculations involve the use of a yield criterion and a flow law. Three yield criteria, each associated with a different elastic-plastic model, are introduced in this section together with the property data and parameters required by each model.

2.2 THE VON MISES MODEL

The simplest yield criterion takes the form [4]

$$\sigma_e = \sigma_T \tag{3}$$

where σ_T is a yield stress in tension and is material property. The criterion assumes that yielding is determined only by the magnitude of the effective shear stress σ_e which is related to principal components of the applied stress σ_1, σ_2 and σ_3 by

$$\sigma_e = \left\{\frac{1}{2}\left[(\sigma_1-\sigma_2)^2 + (\sigma_2-\sigma_3)^2 + (\sigma_3-\sigma_1)^2\right]\right\}^{1/2} \tag{4}$$

Since σ_T varies with plastic strain, equation (3) defines a state of yielding characterised by the tensile stress and the associated level of plastic strain.

2.3 THE LINEAR DRUCKER-PRAGER MODEL

Yielding in polymers is known to be sensitive to the hydrostatic component of stress as well as the shear component [4, 5]. Equation (3) can be extended to include hydrostatic stress sensitivity as follows

$$\sigma_e + \mu\sigma_m = \frac{(\mu+3)}{3}\,\sigma_T = \sigma_o \tag{5}$$

where σ_o is an effective shear yield stress and is a material property and σ_m is the hydrostatic component of stress given by

$$\sigma_m = \tfrac{1}{3}(\sigma_1 + \sigma_2 + \sigma_3) \tag{6}$$

The material parameter μ determines the sensitivity of yielding to hydrostatic stress.

The flow rule is used in elastic-plastic models for the determination of plastic strains through identification of a flow potential F. The most general form for the flow potential in the linear Drucker-Prager model is given by

$$F = \sigma_e + \mu'\sigma_m \tag{7}$$

The flow parameter μ' is a material property that differs from the value of μ in equation (5) if the polymer exhibits non-associated flow. It can be determined from measurement of the plastic component of Poisson's ration ν^p using the expression

$$\mu' = \frac{3(1-2\nu^p)}{2(1+\nu^p)} \tag{8}$$

2.4 THE CAVITATION MODEL

In certain polymers, the yield behaviour under tension is very different from that under compression or shear because of the nucleation of numerous small cavities in the polymer under stress. In the absence of cavitation, equation (5) is a satisfactory

criterion for yielding. Following previous work [2, 6-8], this equation can be modified to include the effects of cavitation as follows

$$\frac{\sigma_e^2}{\sigma_M^2} - (q_1 f)^2 + 2q_1 f \cosh \frac{3\sigma_m}{2\sigma_M} = \left(1 - \frac{\mu\sigma_m}{\sigma_M}\right)^2 \qquad (9)$$

Here f is the effective volume fraction of cavities which at small strains is zero but increases over some characteristic strain region associated with cavity nucleation. Neglecting cavity growth, the maximum value for f is v_C and occurs when cavity nucleation is complete. The value for v_C in semi-crystalline polymers might be expected to vary with molecular orientation and crystallinity. The parameter q_1 has been introduced (2) to account for the effect of void interactions on the stress distribution in the matrix between cavities.

σ_M is the effective yield stress of the matrix polymer between cavities and is equal to σ_o in the absence of cavities. As cavity nucleation proceeds and the rubbery regions become replaced by cavities, σ_M will increase with f. The relationship between σ_M and f will depend upon how the effective shear yield stress of the uncavitated polymer σ_o varies with the volume fraction v_C of the cavitatable phase. The results of experiments and model calculations on an unfilled propylene-ethylene copolymer [9] suggest that this takes the form

$$\sigma_o = \sigma_{MC} \exp\left[-(k\, v_C)\right] \qquad (10)$$

where σ_{MC} is the effective shear yield stress of the material between cavities when cavitation is complete. The expression for σ_M is then given by

$$\sigma_M = \frac{\sigma_o}{\exp\left[-k\, v_C\right]} \exp\left[-k\frac{(v_C - f)}{(1-f)}\right] \qquad (11)$$

From equation (5), $\sigma_o = \sqrt{3}\,\sigma_S$, where σ_S is a yield stress under shear, and is derived from experimental data obtained in shear and replaces σ_T as the basic hardening function for the polymer. The nucleation of a cavity is assumed to occur at some

critical volumetric strain that varies with the size of the cavitatable region. For a distribution of sizes of these regions, the cavity nucleation should occur over a range of total volumetric strain ε_V.

Through comparisons with experimental data for a range of plastics (3), it has been shown that the increase in the volume fraction of nucleated cavities f with volumetric strain is given with satisfactory accuracy by the expressions

$$\begin{aligned} f &= 0 \text{ for } \varepsilon_V \le \varepsilon_{1V} \\ f &= v_C \left\{ 1 - \exp\left[-\left(\frac{\varepsilon_V - \varepsilon_{1V}}{\varepsilon_{2V}} \right)^{\beta} \right] \right\} \text{ for } \varepsilon_V > \varepsilon_{1V} \end{aligned} \tag{12}$$

The parameters ε_{1V}, ε_{2V} and β determine the location and breadth of the volumetric strain range over which cavity nucleation occurs.

The flow potential in this model is, by analogy with equation (7), assumed to be

$$F = \frac{\sigma_e^2}{\sigma_M^2} - (q_1 f)^2 + 2q_1 f \cosh \frac{3\sigma_m}{2\sigma_M} - \left(1 - \frac{\mu' \sigma_m}{\sigma_M} \right)^2 \tag{13}$$

The results of measurements of Poisson's ratio prior to cavity nucleation in tension and under uniaxial compression (where f = 0) indicate that μ' has a relatively low value when f = 0 which then increases with the cavity volume fraction. This observation has lead to the following proposed expression for μ'

$$\mu' = \mu_1' \frac{(1 - v_C)}{(1 - f)} \tag{14}$$

where μ_1' is the value when cavitation is complete.

3 DETERMINATION OF MODEL PARAMETERS

3.1 EXPERIMENTAL

The data requirements for a finite element analysis depend on the choice of materials model used to describe the deformation behaviour of the polymer. Results over a range of test speeds are needed for an analysis with rate-dependent plasticity. For the determination of all the parameters in the cavitation model, measurements of stress/strain curves are needed in tension, shear and compression. Measurements of the variation of Poisson's ratio with tensile strain are also required. The test methods used to determine the results reported here have been described elsewhere [3, 10]. Measurements of tensile modulus and the elastic Poisson's ratio were made on specimens of standard geometry specified in ISO 527-2 [11]. This specimen is not suitable for the determination of tensile stress/strain behaviour at large strains (above the peak in stress) because of strain localisation in the gauge length of the specimen.

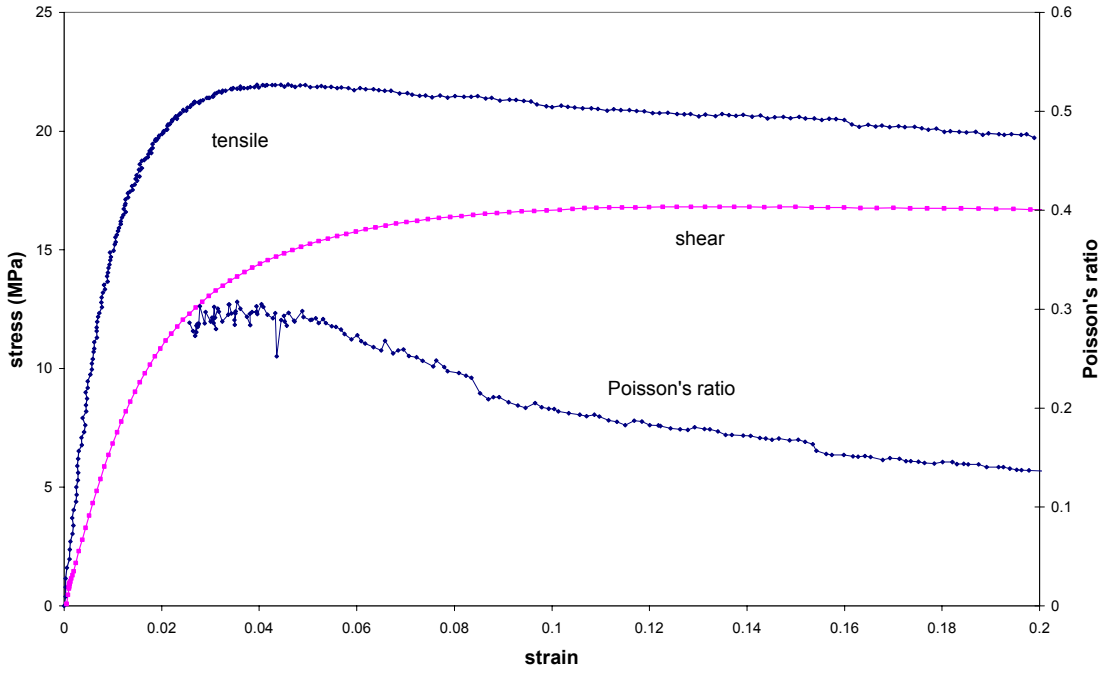

Figure 1. Measurements of tensile and shear behaviour made on specimens cut from a door trim moulding. Strain rate = 0.01 s^{-1}.

A smaller specimen [10], with a central, waisted region to enable the extensometers to be located in the region of strain localisation, was used for the measurement of tensile stress/strain curves. Measurements of stress/strain curves in tension and shear and of

Poisson's ratio are shown in Figure 1. The tensile stresses and strains are true values. Measurements were made on specimens cut from a door trim moulding at test speeds giving a plastic strain rate of 0.01 s^{-1}. This source of material is too thin to enable measurements to be made under uniaxial compression. Compressive stress/strain curves were therefore measured on specimens cut from injection moulded bars, of nominally the same polymer, supplied by Dow Plastics. These specimens were 10 mm square by 4 mm thick which was sufficient to delay buckling in the test until after the peak in compressive stress had been reached. A result at a strain rate of 0.01 s^{-1} is compared with tensile and shear data in Figure 2.

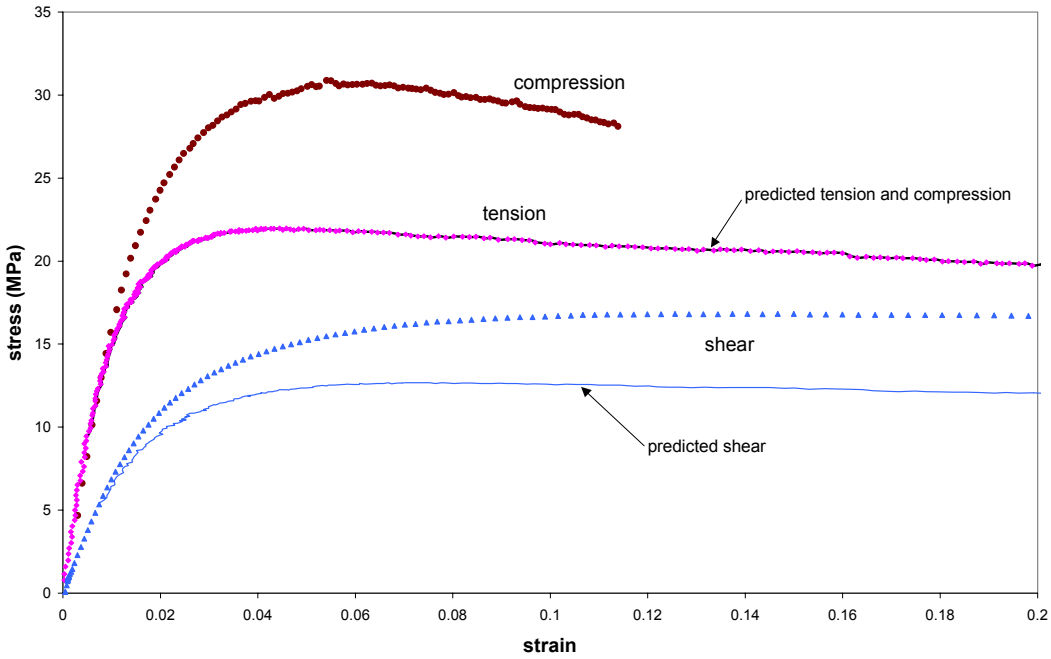

Figure 2. Comparison of compressive and shear stress/strain curves predicted using the von Mises model with experimental data. Continuous lines are predicted values.

Procedures are described next for determining the parameters in each model. Using these parameters, predictions are made of stress/strain curves under tension, shear and compression and of Poisson's ratio for comparison with experimental results to reveal the nature of limitations in the applicability of each model.

3.2 DETERMINATION OF PARAMETERS IN THE VON MISES MODEL

The property requirements for this model have been introduced in section 2.2 and are

- Young's modulus E and elastic Poisson's ratio ν^e
- tensile hardening curves $\sigma_T(\varepsilon_T^p)$ over a range of strain rates.

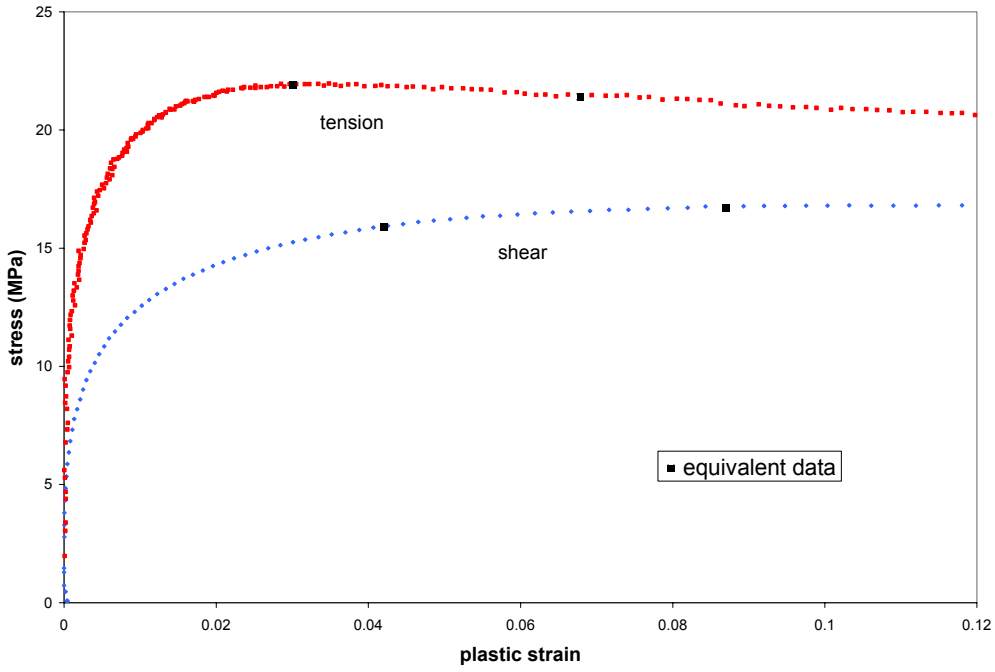

Figure 3. Hardening curves derived from the tensile and shear results in Figure 1.

Values for E and ν^e were obtained from tensile measurements on specimens cut from door panels having the ISO standard geometry. The test speed was 1 mm/s giving an elastic strain rate of 0.01 s^{-1}. There is curvature in these results even at very low strains, arising from the linear viscoelastic behaviour of the polymer. This makes the determination of a Young's modulus ambiguous. The ISO Standard for the determination of tensile properties [11] specifies the gradient of the secant between strains of 0.0005 and 0.0025. This upper strain limit is too low for elastic-plastic analyses which require a strain limit that identifies the onset of significant non-linear behaviour attributable to plastic deformation. We have selected a strain limit of 0.005 for the polymer studied here, giving a value for E = 1.99 GPa. The elastic Poisson's ratio over this strain range is 0.37. The hardening curve at this strain rate was derived

from the tensile measurements in Figure 1. The elastic component of strain was deducted using equation (2) to give the hardening curve $\sigma_T(\varepsilon_T^p)$ shown in Figure 3. The determination of hardening curves at higher strain rates is described in section 4.2.

These results are sufficient to enable the von Mises elastic-plastic model to be used to predict stress/strain curves under uniaxial compressive and shear stresses and the variation of Poisson's ratio with strain. These predictions are compared with experimental data in Figures 2 and 4. In Figure 2, it can be seen that the predicted compressive behaviour coincides with the tensile data and the shear prediction lies below experimental values. In addition, the fall in Poisson's ratio with strain is not predicted by the model, as shown in Figure 4. These observations are a direct consequence of the neglect, in the von Mises model, of any influence of the hydrostatic component of the applied stress on yield behaviour. If higher accuracy in predictive capability is required, alternative models should be considered.

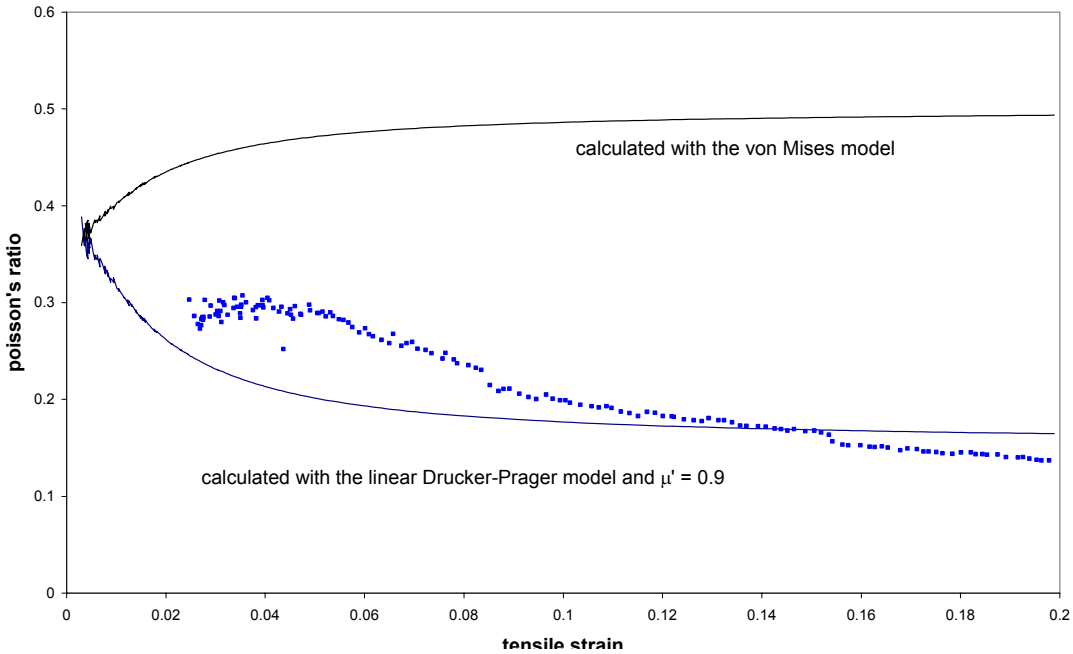

Figure 4. Comparison of Poison's ratio measurements with values predicted using the von Mises and linear Drucker-Prager models.

3.3 DETERMINATION OF PARAMETERS IN THE LINEAR DRUCKER-PRAGER MODEL

The property requirements for this model have been introduced in section 2.3 and are

- Young's modulus E and elastic Poisson's ratio ν^e
- tensile hardening curves $\sigma_T(\varepsilon_T^p)$ over a range of strain rates
- the hydrostatic stress sensitivity parameter μ
- the flow parameter μ'.

The first two requirements are identical to those for the von Mises model reported in section 4.2. Determination of the parameter μ requires the measurement of hardening behaviour under an additional stress state. Measurements under shear, although not routine, are probably achievable with greater precision than under uniaxial compression. The shear hardening curve for the door trim has been calculated from the shear data in Figure 1 and compared with the tensile hardening curve at the same effective plastic strain rate in Figure 3. Points σ_T, ε_T^p lie on the tensile curve and points σ_S, ε_S^p lie on the shear curve.

According to the linear Drucker-Prager criterion equation (5), equivalent stresses σ_S and σ_T are related by the expression

$$\sqrt{3}\,\sigma_S = \sigma_T(\mu+3)/3 \tag{15}$$

which gives

$$\mu = 3\left[\left(\sqrt{3}\,\sigma_S/\sigma_T\right)-1\right] \tag{16}$$

where equivalent stresses σ_S and σ_T satisfy the equation

$$\sigma_T\,\varepsilon_T^p = \sigma_S\,\varepsilon_S^p \tag{17}$$

The value for μ derived using equation (16) depends upon which pair of equivalent stresses are selected from the curves in Figure 3 and lies in the range 0.8 at low plastic

strain to 1.0 at higher strains. Using a value for μ of 1.0 together with the tensile hardening curve in Figure 3 and elastic properties, predictions of shear and compressive stress/strain curves made with the linear Drucker-Prager model are compared with experimental data in Figure 5. Whilst the predicted shear behaviour is reasonable, the predicted compressive curve is much higher than experimental values.

A value for the flow parameter μ′ can be derived from measurement of the plastic component of Poisson's ratio using equation (8). A value for ν^p can be calculated from the data for Poisson's ratio in Figure 1 using the equation

$$\nu^p = \frac{\nu\varepsilon_T - \nu_e\sigma/E}{\varepsilon_T - \sigma/E} \tag{18}$$

This gives a value for $\nu^p = 0.12$ and thus a value for μ′ of 0.9, as recorded in Table 1. Using this value for μ′, the dependence of Poisson's ratio with strain predicted by the linear Drucker-Prager model is compared with measured values in Figure 4.

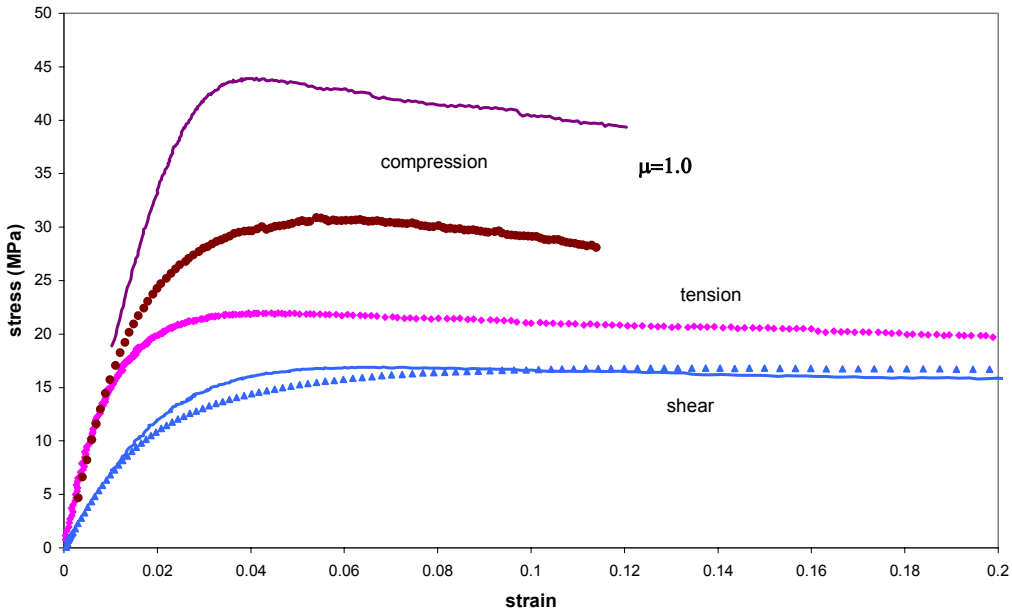

Figure 5. Comparison of measured compressive and shear stress/strain results (data points) with curves (solid lines) predicted using the linear Drucker-Prager model with μ = 1.0.

Figures 4 and 5 illustrate the limitations in the linear Drucker-Prager model for describing the elastic-plastic behaviour of this polymer and the associated uncertainty in the derivation of appropriate values for the model parameters. For an approximate analysis using this model, the set of parameters listed in Table 1 are considered likely to give an acceptable description of elastic-plastic behaviour in typical situations.

Table 1 Typical values for the parameters in the linear Drucker-Prager model at a strain rate of 0.01 s^{-1}

E (GPa)	1.99
ν^e	0.37
$\sigma_T(\varepsilon_T^p)$ (MPa)	fig 3
μ	1.0
μ'	0.9

3.4 DETERMINATION OF PARAMETERS FOR THE CAVITATION MODEL

3.4.1 General

The inability of the linear Drucker-Prager model to accurately describe both shear and compressive behaviour and the fall in Poisson's ratio with strain arises because the model does not take account of the nucleation of numerous small cavities on the yield behaviour under a tensile stress. These cavities nucleate over a range of tensile strain, and this gives rise to the different shape of the tensile curve compared with either the shear or compressive curves as seen in Figure 5 where the tensile hardening curve is used to predict shear and compressive behaviour. The cavitation model attempts to include the influence of cavitation on deformation behaviour through adaption of the yield criterion and the introduction of a cavity nucleation criterion that relates the volume fraction of nucleated cavities to the magnitude of the volumetric strain.

The property requirements for this model have been introduced in section 2.4 and are

- Young's modulus E and elastic Poisson's ratio ν^e
- effective shear hardening curves $\sigma_o(\varepsilon_o^p)$ over a range of strain rates. These replace tensile hardening curves in the previous models.

- a hydrostatic stress sensitivity parameter μ
- the volume fraction of cavities v_C in the fully cavitated material
- a cavity interaction parameter q_1
- parameters σ_{MC} and k in equation (10) that describes how the effective shear yield stress σ_o varies with the volume fraction of the phase in which cavities can form
- parameters ε_{1V}, ε_{2V} and β in equation (12) that relates the volume fraction of nucleated cavities f to the volumetric strain produced by the applied stress
- a flow parameter μ'.

3.4.2 The effective shear hardening behaviour $\sigma_o(\varepsilon_o^p)$

For the cavitation model, hardening behaviour is expressed by a curve of the effective stress σ_o against the effective plastic strain ε_o^p. These quantities are obtained from shear stress (σ_S) and shear strain (ε_S) data in Figure 5 using the relationships

$$\sigma_o = \sqrt{3}\,\sigma_S$$

and

$$\varepsilon_o^p = \varepsilon_S^p / \sqrt{3} \qquad (19)$$

where ε_S^p is the plastic component of the shear strain and is given, by analogy with equation (2), by

$$\varepsilon_S^p = \varepsilon_S - \frac{\sigma_S}{G} \qquad (20)$$

where G is the shear modulus.

The hardening curve for the effective stress at a strain rate of 0.01 s^{-1} has been derived from the shear data in Figure 1 and is shown in Figure 6.

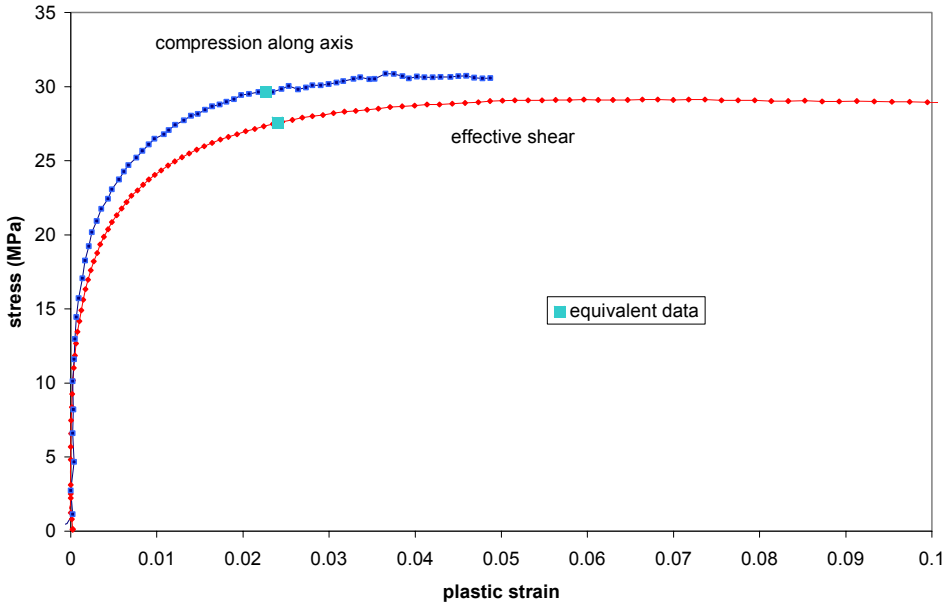

Figure 6. Hardening curves in shear and compression derived from the data in Figures 1 and 2.

3.4.3 The hydrostatic stress sensitivity parameter μ.

Under stress states where no cavities are produced, f = 0 and the yield criterion equation (9) reduces to

$$\frac{\sigma_e}{\sigma_o} = 1 - \frac{\mu \sigma_m}{\sigma_o} \tag{21}$$

It follows that a value for μ can be derived from measurements of yield stresses under shear and compression using the equation

$$\mu = 3(1 - \sigma_o / \sigma_C) \tag{22}$$

The compressive hardening curve $(\sigma_C, \varepsilon_C^p)$ derived from the compression results using specimens cut from injection moulded bars (Figure 2) is compared with the effective shear hardening curve $(\sigma_o, \varepsilon_o^p)$ in Figure 6. Equivalent stresses σ_o, σ_C are

identified to satisfy the plastic work equivalence equation (analogous to equation (17))

$$\sigma_C \, \varepsilon_C^p = \sigma_o \, \varepsilon_o^p \tag{23}$$

A pair of equivalent stresses is shown in Figure 6 and, from equation (22), gives a value for μ of 0.21.

3.4.4 The volume fraction of cavities v_C when cavitation is complete.

The volume fraction of cavities v_C is difficult to estimate because of the variety of sites in the polymer at which cavities could nucleate. A good estimate for v_C can be obtained from accurate Poisson's ratio measurements at strain levels where cavity nucleation is almost complete. According to the cavitation model, when cavity nucleation is complete, the plastic component of Poisson's ratio is given by

$$\nu^p = \frac{\left[\dfrac{\sigma_T}{\sigma_{MC}} - q_1 v_C \sinh\left(\dfrac{\sigma_T}{2\sigma_{MC}}\right) - \dfrac{2\mu_1'}{3}\left(1 - \dfrac{\mu_1' \sigma_T}{3\sigma_{MC}}\right)\right]}{\left[\dfrac{2\sigma_T}{\sigma_{MC}} + q_1 v_C \sinh\left(\dfrac{\sigma_T}{2\sigma_{MC}}\right) + \dfrac{2\mu_1'}{3}\left(1 - \dfrac{\mu_1' \sigma_T}{3\sigma_{MC}}\right)\right]} \tag{24}$$

where σ_{MC} and μ_1' are values for σ_M and μ' when cavitation is complete, see equations (11) and (14). The yield criterion (equation (9)) under these conditions with a tensile applied stress gives

$$\frac{\sigma_T^2}{\sigma_{MC}^2} - (q_1 v_C)^2 + 2 q_1 v_C \cosh\left(\frac{\sigma_T}{2\sigma_{MC}}\right) - \left(1 - \frac{\mu \sigma_T}{3\sigma_{MC}}\right)^2 = 0 \tag{25}$$

Equation (25) shows that the ratio σ_T/σ_{MC} is determined predominantly by the magnitude of $q_1 v_C$. This means that, from equation (24), the value for Poisson's ratio is determined by the quantities $q_1 v_C$ and μ_1'. Previous studies in which the cavitation model has been applied to the results of tests on a rubber toughened glassy polymer

ABS [3] and a propylene-ethylene copolymer [9], reveal that the parameters q_1 and μ_1' are difficult to determine with any precision and may be broadly independent of the polymer material. We therefore take typical values for $q_1 = 1.5$ and $\mu_1' = 0.17$. It is now possible to use equation (24) to calculate the variation of Poisson's ratio with tensile strain for different values of v_C for comparison with experimental data. A good comparison is shown in Figure 7 using a value of $v_C = 0.47$.

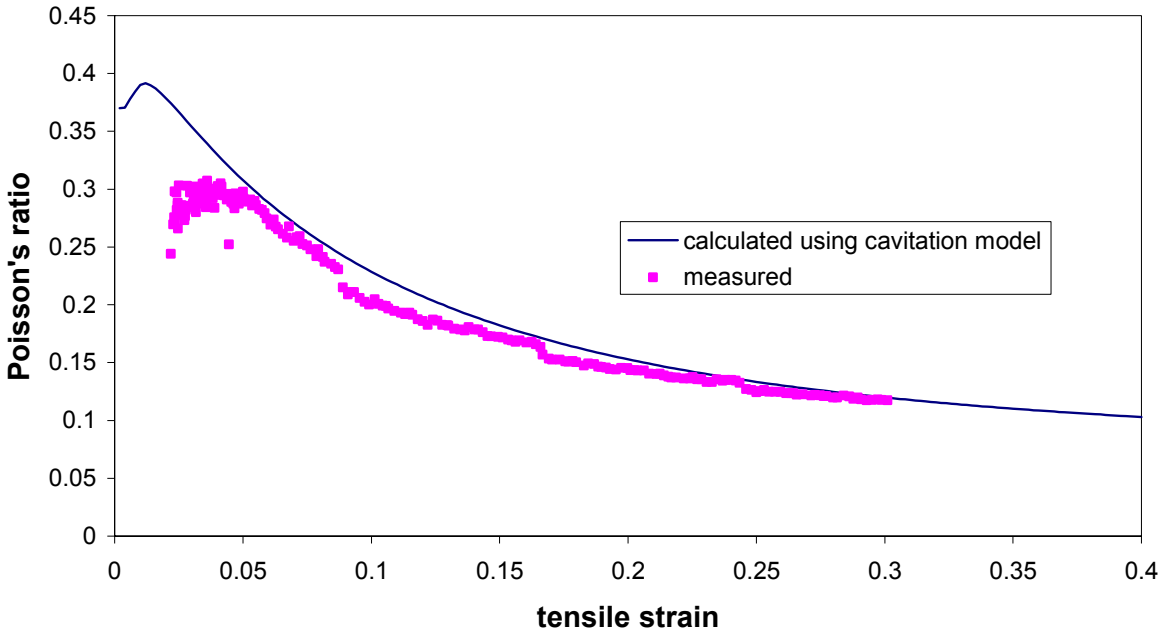

Figure 7. Comparison of measured values of Poisson's ratio with predictions using the cavitation model with a value for $v_C = 0.47$.

3.4.5 Parameters ε_{1v}, ε_{2v}, β and k

These parameters are obtained by an iterative process to achieve satisfactory predictions of the shape of the tensile stress/strain curve in the strain range associated with cavity nucleation. This requires a method for obtaining solutions to equations (9), (11) and (12) for the case of uniaxial tension for comparison with experiment. The solutions can be achieved by a finite element analysis applied to a single element with appropriate boundary conditions, but a routine coded on a PC is more convenient. An optimisation procedure for finding the parameter values is not necessary since this is best done by an interactive method for rapidly exploring the

effect of changes to the parameters on curve shapes. Figure 8 shows a comparison of measured and calculated tensile curves obtained using the parameters listed in Table 2.

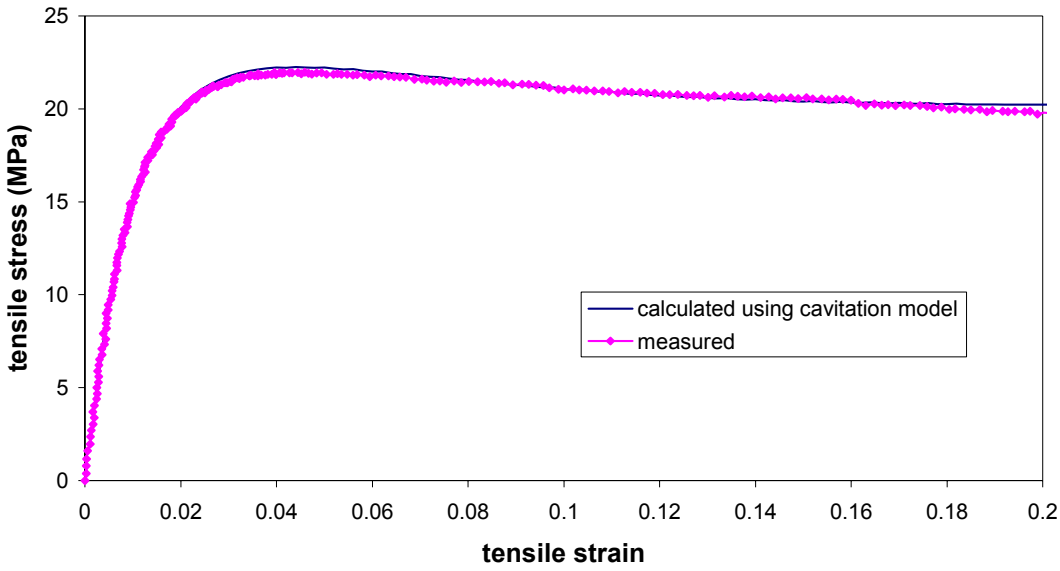

Figure 8. Comparison of the measured tensile curve at a strain rate of 0.015 s^{-1} with predictions using the cavitation model and parameter values listed in Table 2.

Table 2 Values for parameters in the cavitation model at a strain rate of 0.01 s^{-1}

E (GPa)	1.99
ν^e	0.37
$\sigma_o\left(\varepsilon_o^p\right)$ (MPa)	fig 6
μ	0.21
ν_C	0.47
K	2.55
σ_{MC} (MPa)	96 (from eqn (10))
q_1	1.5
μ_1'	0.17
ε_{1v}	0.0022
ε_{2v}	0.01
β	0.5

4 RATE DEPENDENT PLASTICITY

4.1 GENERAL

Whichever model is used for a stress analysis, more accurate predictions will be made if the dependence of properties on strain rate is taken into consideration. In many finite element systems, facilities are available for including the dependence of yield behaviour on strain rate (rate-dependent plasticity) characterised by a series of hardening curves at different strain rates. However, there are experimental problems with the measurement of these properties at the high strain rates associated with impact events (> 100 s^{-1}). A procedure used here for the determination of properties at high strain rates involves:

- modelling the shape of experimental hardening curves at low and moderate strain rates
- determining the variation of model parameters with strain rate
- and deriving hardening behaviour at high strain rates by extrapolation.

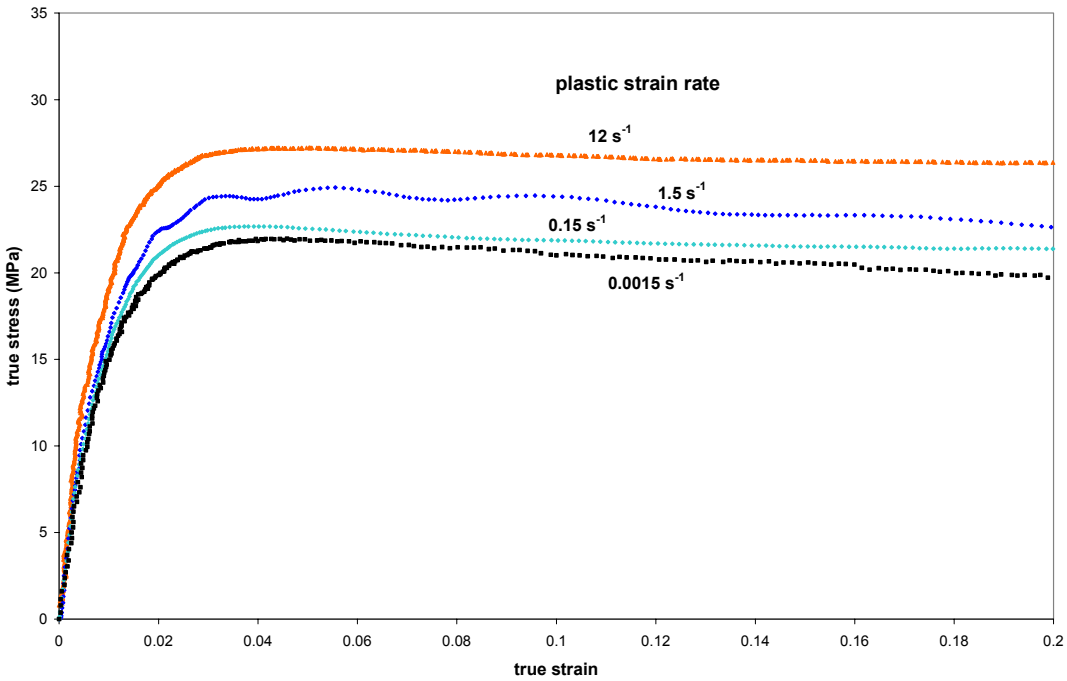

Figure 9. Tensile stress/strain curves measured at the strain rates shown.

4.2 TENSILE BEHAVIOUR

Tensile tests were carried out on the waisted specimen geometry referred to in section 3.1 at test speeds ranging from 0.1 mm/s to 100 mm/s. These tests gave plastic strain rates in the range 0.01 s^{-1} to 10 s^{-1}. Specimens were cut from several door trim mouldings and from different regions within each moulding. The reproducibility in measurements at each test speed was within ± 1 MPa in the value of the stress at peak. Typical stress/strain curves at different rates are shown in Figure 9. The indicated strain rates are true plastic strain rates determined from strain vs time plots at a strain level where the deformation is predominantly plastic. Hardening curves $\sigma_T(\varepsilon_T^p)$ derived from these data are shown in Figure 10.

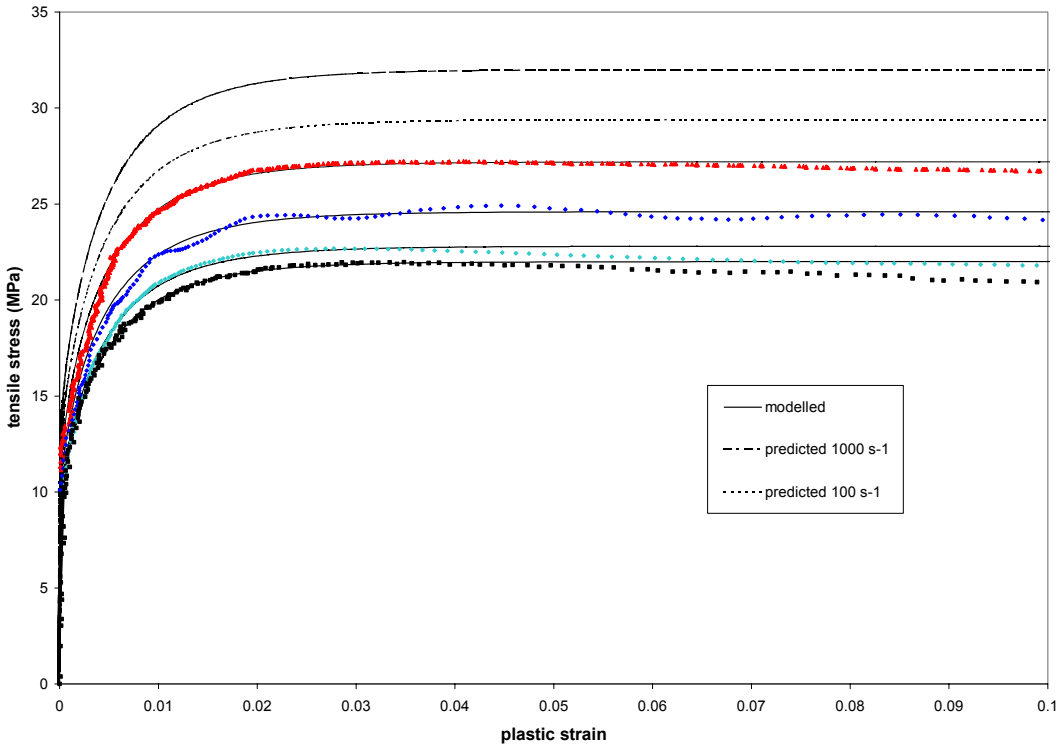

Figure 10. Tensile hardening curves derived from the results in Figure 9 modelled using equation (26) with the parameters in table 3. The 2 curves at the highest strain rates were then derived by calculation using equations (26) and (27) and the parameters in Table 6.

These curves have been fitted using the function

$$\sigma_T(\varepsilon_T^p) = \sigma_i + (\sigma_f - \sigma_i)\left(1 - \exp -(\varepsilon_T^p / \varepsilon_a)^\beta\right) \qquad (26)$$

where σ_i is the stress at zero plastic strain, σ_f is the limiting stress at high plastic strains and ε_a and β are parameters that determine the mean strain and the strain range over which the increase of σ_T with ε_T^p occurs. Values for the parameters used to obtain the fits in Figure 10 are shown in Table 3. The data in Table 3 show that the main parameter to change with strain rate is the flow stress σ_f. The initial yield stress σ_i also increases with rate, but, to a good approximation, $\sigma_i = 0.4\sigma_f$, independent of rate. The parameter β is effectively constant.

Table 3 Values for the parameters in equation (26) used to obtain the fits to tensile data in Figure 10

Plastic strain rate (s^{-1})	σ_f (MPa)	$\sigma_i = 0.4\ \sigma_f$	ε_a	β
12	27.2	10.9	0.0045	0.8
1.5	24.6	9.8	0.0045	0.8
0.15	22.8	9.1	0.0045	0.8
0.015	22.0	8.8	0.0045	0.8

Tensile stress/strain curves similar to those shown in Figures 9 and 10 have been obtained in other work [10, 12] on injection moulded specimens, which give significantly more reproducible results because of higher consistency in the structure of the polymer in the specimens. Analysis of these measurements reveals that the increase in the flow stress σ_f with strain rate can be accurately modelled by the Eyring function.

$$\sigma_f = \sigma_{fo} + A \log \dot{\varepsilon}_T^p \qquad (27)$$

where σ_{fo} and A are material parameters. The values for σ_f recorded in Table 3 have been plotted against log strain rate in Figure 11. Using equation (27) to model these data gives values for σ_{fo} = 24.7 MPa and A = 1.9 MPa when strain rate is in units of s^{-1}.

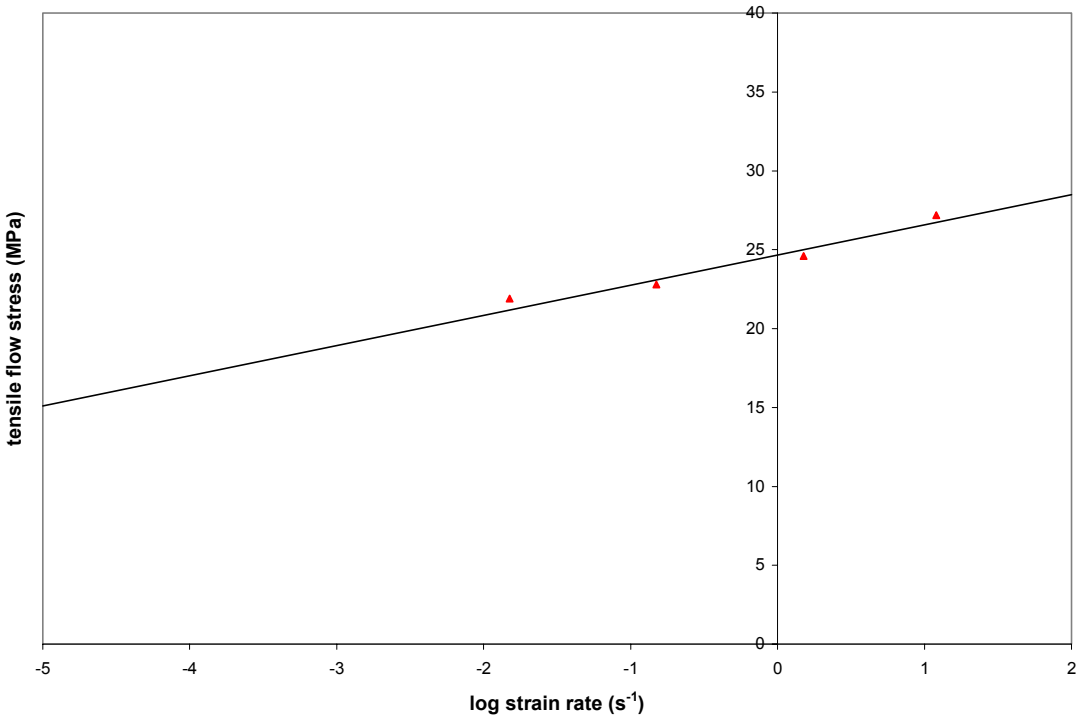

Figure 11. Plots of flow stresses in tension obtained from the fits to experimental data in Figure 10 against the log of the strain rate.

Equations (26) and (27) together with a knowledge of 5 material parameters (σ_{fo}, A, σ_i/σ_f, ε_a and β) can therefore be used to derive tensile hardening curves at any arbitrary strain rate. This information constitutes the hardening properties required by an analysis with rate dependent plasticity using the von Mises or linear Drucker-Prager models. (Note, the cavitation model requires hardening properties in the form of effective shear data (see section 4.3)). The origin of the predicted curves at the highest strain rates in Figure 10 is discussed in section 4.3.

4.3 SHEAR BEHAVIOUR

Plastic strain hardening in the cavitation model is defined by hardening curves determined under a shear stress (see sections 2.4 and 3.4.2). Stress/strain curves measured in shear at different strain rates are shown in Figure 12. Hardening behaviour is expressed by a curve of the effective stress σ_o against the effective plastic strain ε_o^p which are related to shear stress and strain values by equations (19)

in section 3.4.2. Hardening curves for the effective stress have been derived from the data in Figure 12 and are shown in Figure 13.

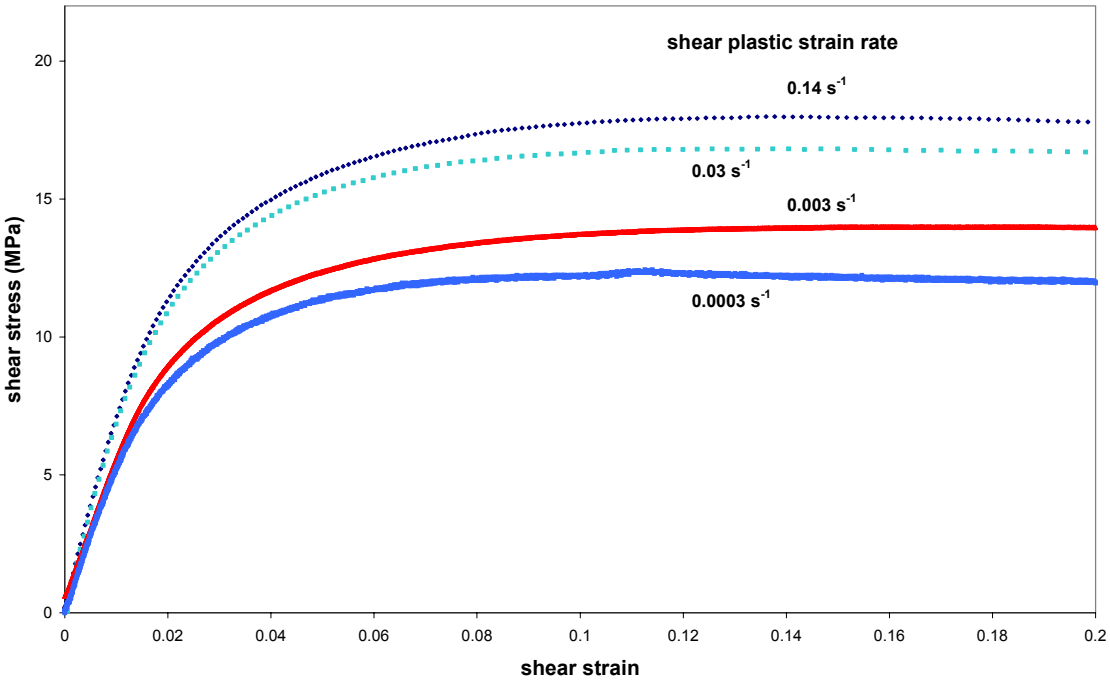

Figure 12. Shear stress/strain curves measured at different strain rates.

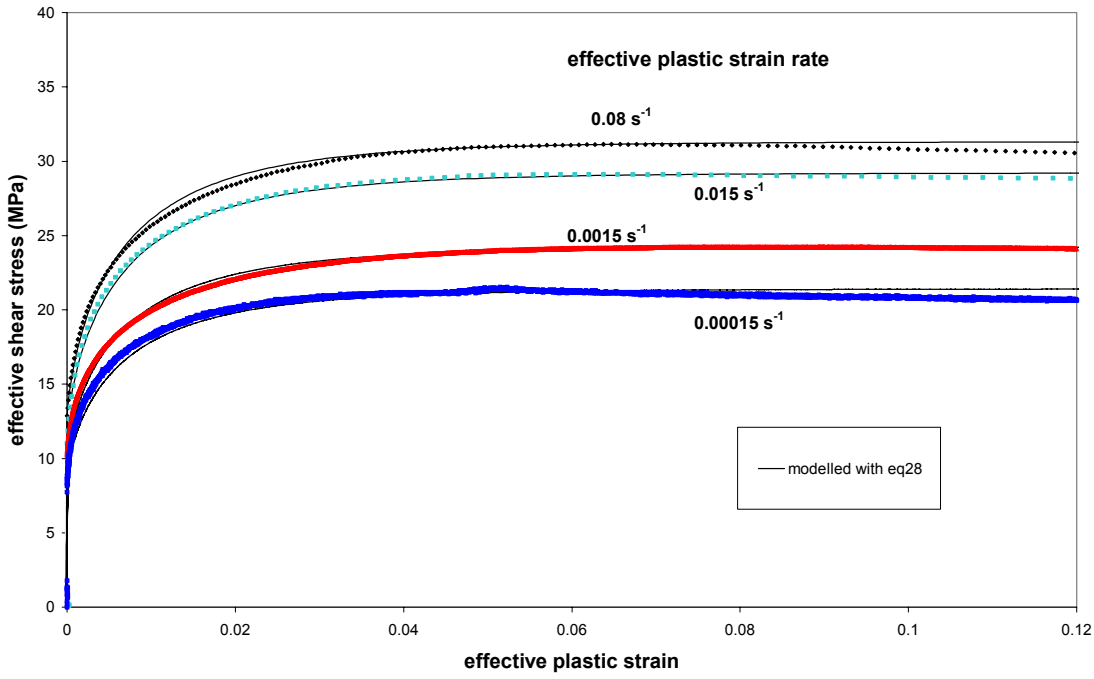

Figure 13. Effective shear hardening curves derived from the results in Figure 12 and modelled using equation (28) with the parameters in Table 4.

The shear curves in Figure 13 have been modelled using the following equation, which has the same form as equation (26) that was used to model hardening under tension,

$$\sigma_o(\varepsilon_o^p) = \sigma_{oi} + (\sigma_{of} - \sigma_{oi})\left(1 - \exp - (\varepsilon_o^p / \varepsilon_{oa})^{\beta_o}\right) \qquad (28)$$

where σ_{oi} is the stress at zero plastic strain, σ_{of} is the limiting stress at high plastic strains and ε_{oa} and β_o are parameters that determine the mean strain and the strain range over which the increase of σ_o with ε_o^p occurs. Values for the parameters in equation (28) are shown in Table 4.

Table 4 Values for the parameters in equation (28) used to fit the shear data in Figure 13

Effective plastic strain rate (s^{-1})	σ_{of} (MPa)	σ_{oi} (MPa)	ε_{oa}	β_o
0.08	31.3	12.5	0.007	0.7
0.015	29.2	11.6	0.007	0.7
0.0015	24.2	9.7	0.007	0.7
0.00015	21.4	8.6	0.007	0.7

It can be seen from the results in Table 4 that the ratio σ_{oi}/σ_{of} may be assumed constant at a value of 0.4 as with the tensile data in Table 3. Values for σ_{of} from Table 4 are plotted against log plastic strain rate in Figure 14 and are compared with the tensile data from Figure 11. The broken line in this figure is the fit to these tensile data shown in Figure 11. The variation of the shear flow stress σ_{of} with log strain rate $\dot{\varepsilon}_o^p$ can be represented by a straight line having the equation, analogous to equation (27),

$$\sigma_{of} = \sigma_{ofo} + C \log \dot{\varepsilon}_o^p \qquad (29)$$

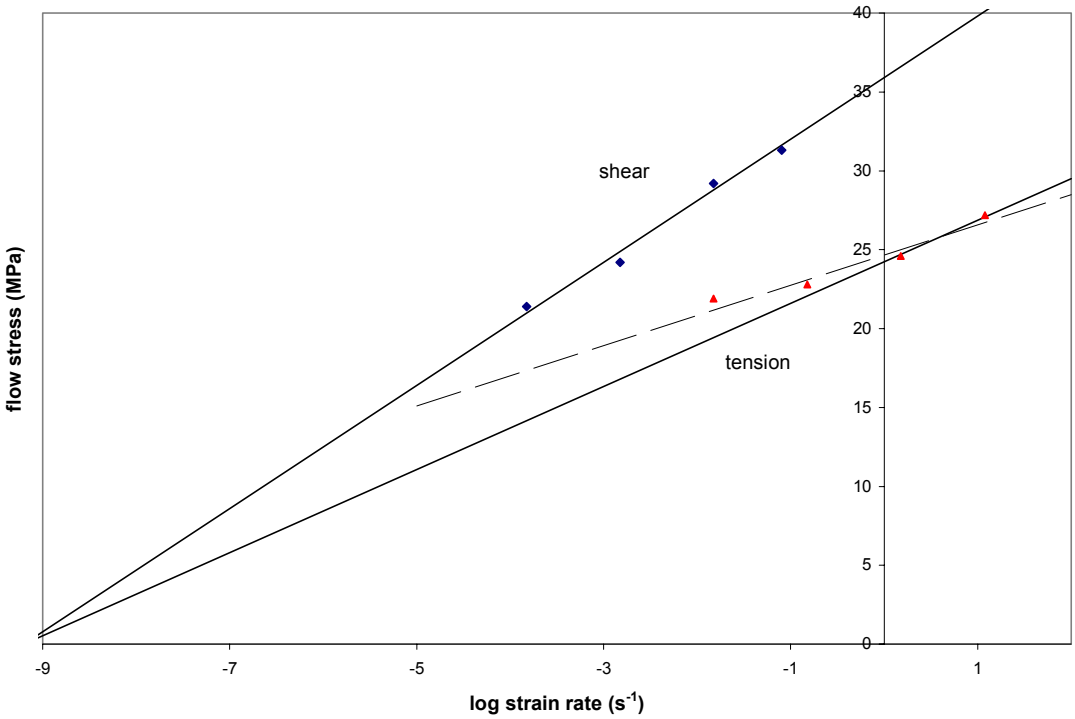

Figure 14. Plots of flow stresses for tensile and shear tests from Tables 3 and 4 against log of the strain rate.

Values for the parameters in equations (28) and (29) are recorded in Table 5. These have been used to determine effective shear hardening curves at any strain rate in finite element analyses using the cavitation model.

Table 5 Values for the parameters in equations (28) and (29) used to model rate-dependent plasticity in shear for the cavitation model

σ_{ofo} (MPa)	35.9
C (MPa)	3.9
σ_{oi} (MPa)	0.4 σ_{of}
ε_{oa}	0.007
β_o	0.7

The results in Figure 14 do not have a common intercept on the log strain rate axis. The ratio of tensile and effective shear flow stresses therefore varies with strain rate.

The probable reason for this is that the cavity volume fraction when cavity nucleation is complete increases with strain rate. This conclusion is supported by measurements of Poisson's ratio at very low test speeds. These results for Poisson's ratio show a smaller drop in value than is observed in results at higher speeds (see Figure 4) which is consistent with a lower value for v_C. As the strain rate is lowered, the shear yield stress decreases thereby promoting shear yielding in favour of cavitation in certain regions of the polymer. At higher rates, cavitation takes place in these regions but there will presumably be a limit to the increase in v_C with strain rate when cavities have formed in all the available regions in the polymer. This means that, at higher strain rates, the gradient of the tensile line should increase thereby introducing some uncertainty in the linear extrapolation of equation (29).

The main implication of this conclusion is that some of the parameters in both linear Drucker-Prager and the cavitation models will vary with strain rate. In the case of the Drucker-Prager model, it is the parameter μ that will increase with increasing rate. The value recorded in Table 1 has been derived from tensile and shear data at a strain rate of 0.015 s^{-1}. It is not known whether the value will be significantly higher at higher strain rates. With the cavitation model, apart from the parameter v_C, there may be small associated changes in the nucleation parameters ε_{1v}, ε_{2v} and β. In the finite element analyses carried out no account is taken of the possible variation of these parameters with rate. In order to minimise errors in the determination of hardening behaviour at high strain rates by extrapolation of the tensile data in Figure 14, the continuous line in Figure 14 has been drawn through the data at the higher strain rates and through the intersection of the shear line with the log strain rate axis. This line represents behaviour for which v_C is independent of rate and is consistent with a value for v_C at high rates. This line has been used to derive the parameters in equation (27) used to calculate rate-dependent hardening in tension. Values for the parameters in equations (26) and (27) are recorded in Table 6. These have been used with equations (26) and (27) to predict the hardening curves at the higher strain rates in Figure 10, associated with impact events.

Table 6 Values for the parameters in equations (26) and (27) used to model rate-dependent plasticity in tension

σ_{fo} (MPa)	24.2
A (MPa)	2.6
σ_i (MPa)	0.4 σ_f
ε_a	0.0045
β	0.8

5 TESTS ON SUBCOMPONENTS

The door trim panels used in this work are manufactured by extrusion compression moulding. Two subcomponent parts were selected and cut from the mouldings. The locations of the subcomponents within the moulding are shown in Figure 15. The armrest subcomponent (labelled A in Figure 15) is part of the armrest region. The region labelled B in Figure 15 is a curved area cut from the upper boundary of the panel and is stiffened by ribs. This part was referred to as the toptrim.

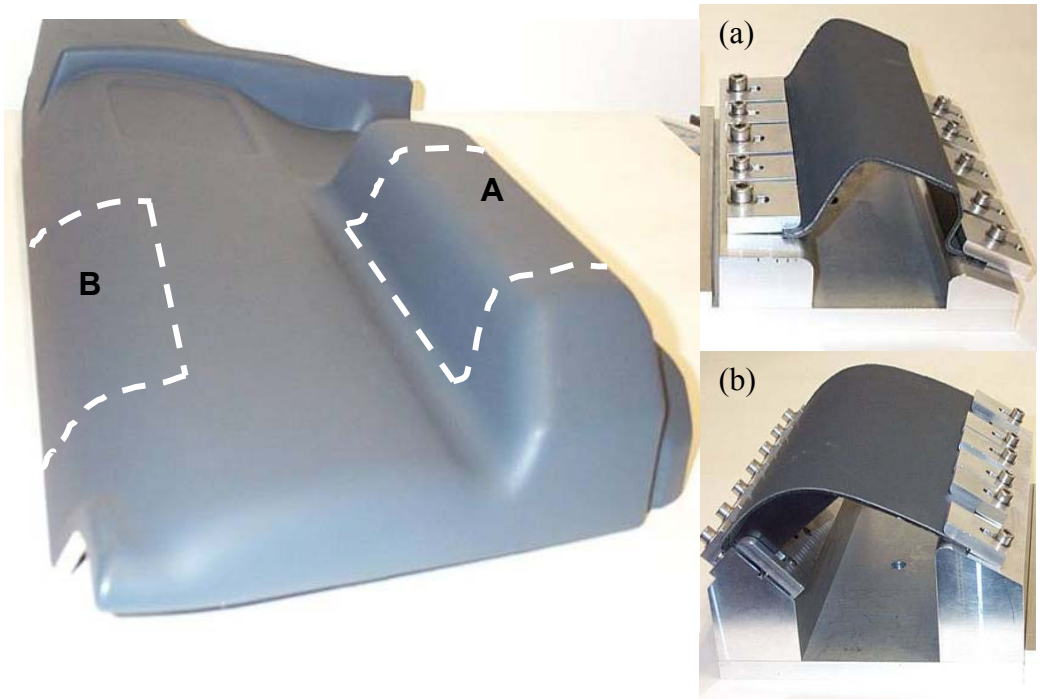

Figure 15. Door trim panel with component positions A (armrest) and B (toptrim) marked. Also shown are the clamping devices for (a) armrest and (b) toptrim.

Clamping devices have been manufactured in-house to support some of the boundaries of each subcomponent specimen under conditions that can be simulated in the FE analyses. The subcomponent specimens are loaded in a universal testing machine by a hemispherical surface of diameter 80 mm acting on the centre of the exposed surface of each subcomponent as shown in Figures 15a and 15b. The armrest clamping device is supported at an angle so that the surface to be indented is horizontal. Measurements are made of the force applied by the hemisphere and the displacement of the hemisphere into the surface of the subcomponent. Tests have been carried out at three speeds, 0.1 mm/s, 10 mm/s and 1 m/s. The resulting force-displacement curves for the toptrim component are shown in Figure 16. The curves demonstrate that it is more difficult to obtain smooth data at high rates such as 1 m/s.

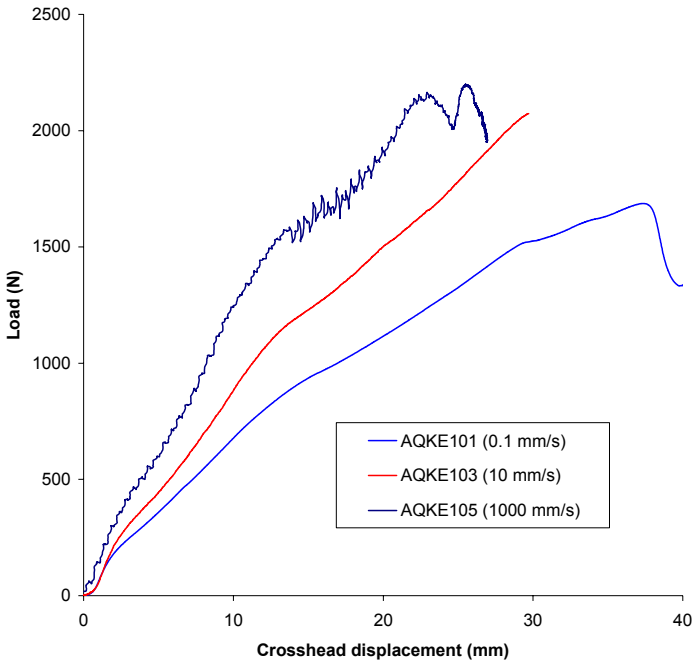

Figure 16. Typical force-displacement plots obtained from toptrim components loaded a three test speeds: 0.1mm/s, 10 mm/s and 1 m/s.

For one set of tests on each component loaded at 0.1 mm/s, digital photographs were taken every 10 seconds. The armrest component was photographed front-on. The toptrim clamping jig was modified allowing camera access beneath the component enabling photographs of the deforming ribs to be obtained.

The force-displacement curves obtained for the toptrim component (Figure 16) show a number of slight changes in slope, or ‘kinks’. Photographs were used to examine the cause of these kinks in the 0.1 mm/s speed tests. The first kink at approximately 2 mm was found to relate to the onset of bending of the main central ribs, see Figure 17. The second kink occurs at a displacement of about 13 mm. It was thought that this would tie in with the onset of deformation of the next pair of ribs. The photographic evidence suggests that contrary to this, the change in slope actually occurs due to a change in the deformation rate of the central ribs. After 12 mm indentation, the central ribs had reached the deformation stage shown in figure 18a. A further indentation of only 2 mm caused a marked increase in bending of the central ribs, see Figure 18b. The third kink, which occurs at a displacement of approximately 28 mm, is due to the initiation of tearing at the base of the central ribs (Figure 18c). This tearing continues with further indentation.

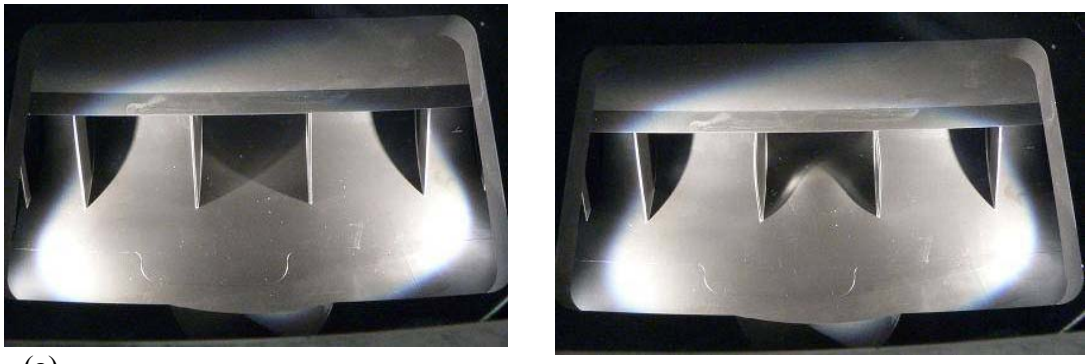

Figure 17. Photographs of the underside of the toptrim component. Photograph (a) was taken at the start of the test, photograph (b) after 2.5 mm displacement.

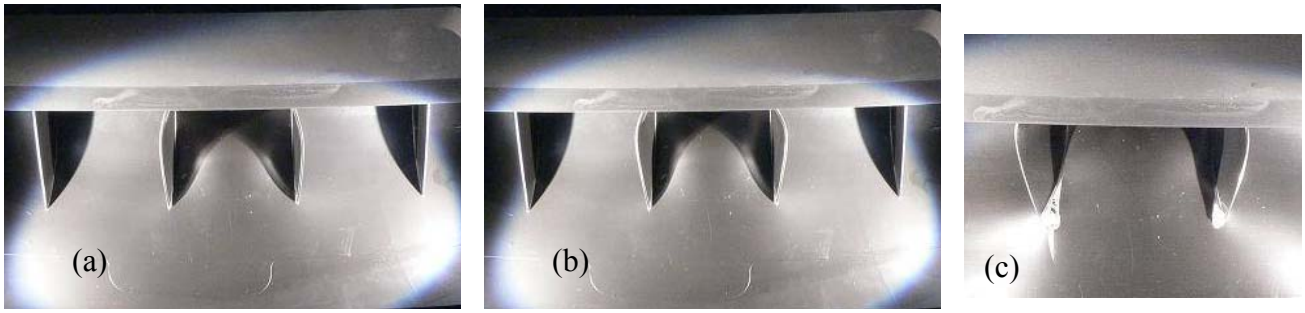

Figure 18. Photographs of the toptrim component taken after (a) 12 mm, (b) 14 mm and (c) 28 mm.

Examination of the photographs from different toptrim components showed differences in the deformed shape of the ribs. This is illustrated in Figure 19 where the left hand rib bends in opposite directions in Figures 19a and 19b. The force-displacement curves obtained from these two components are compared with a third in Figure 19c. There is minimal difference between the curves indicating that the actual deformed shape of the ribs is not important.

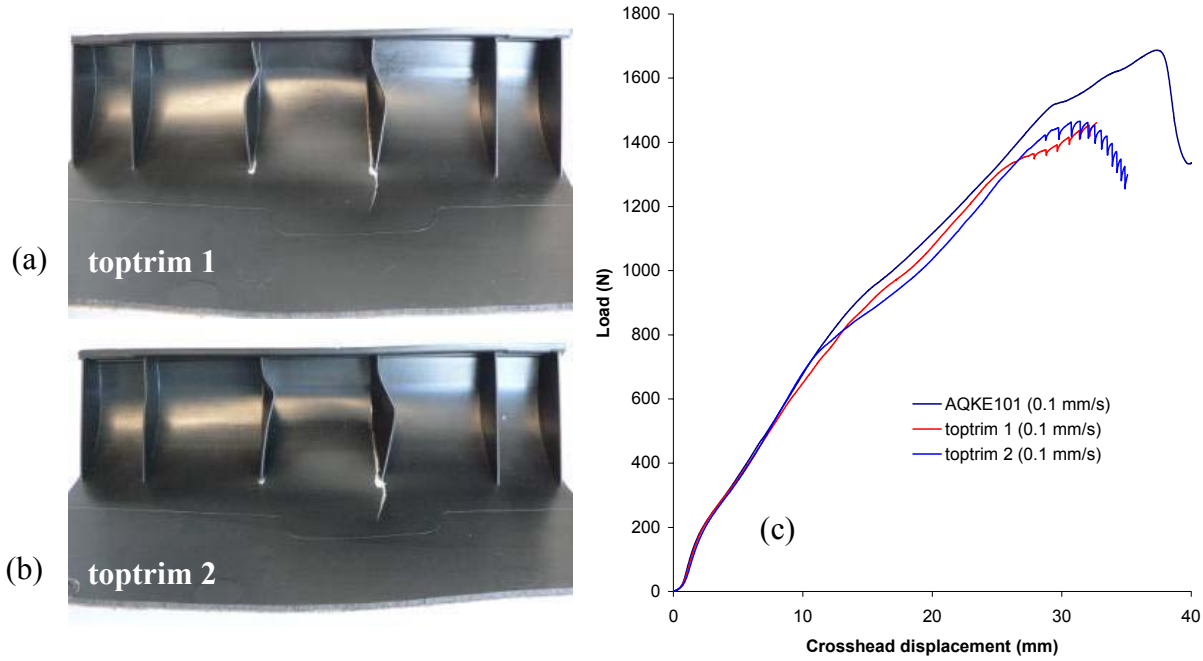

Figure 19. Photographs of two toptrim components (a) and (b) after testing. The graph (c) shows the force-displacement data obtained from these two components and one other toptrim component.

6 FINITE ELEMENT ANALYSIS

6.1 SUBCOMPONENT GEOMETRIES

Finite element analyses were carried out on the door trim subcomponent parts shown in Figure 15 using the software package ABAQUS (ABAQUS Ltd). 3-D geometries of the two components were generated using FEMGV (Femsys Ltd) and were meshed with the solid, continuum elements C3D8R, see Figure 20. An analytical rigid surface was used to describe the indenter geometry, as this is the simplest method of representing the hard indenter. A reference node controls the motion of the indenter, and it is at this node that the predicted force and displacement are obtained. Boundary

conditions were applied to the meshes to replicate the constraints imposed by the clamping devices. Contact surfaces were set up between the rigid surface of the indenter and the top surface of the door trim components. The explicit solver was used for the analyses due to the loading rates investigated, as explicit is designed for modelling high speed and/or high deformation events. Analyses were carried out using the von Mises, linear Drucker-Prager and cavitation models detailed in section 2. The first two are available in ABAQUS. Separate coding was developed for implementing the cavitation model as a user material model (UMAT) within ABAQUS.

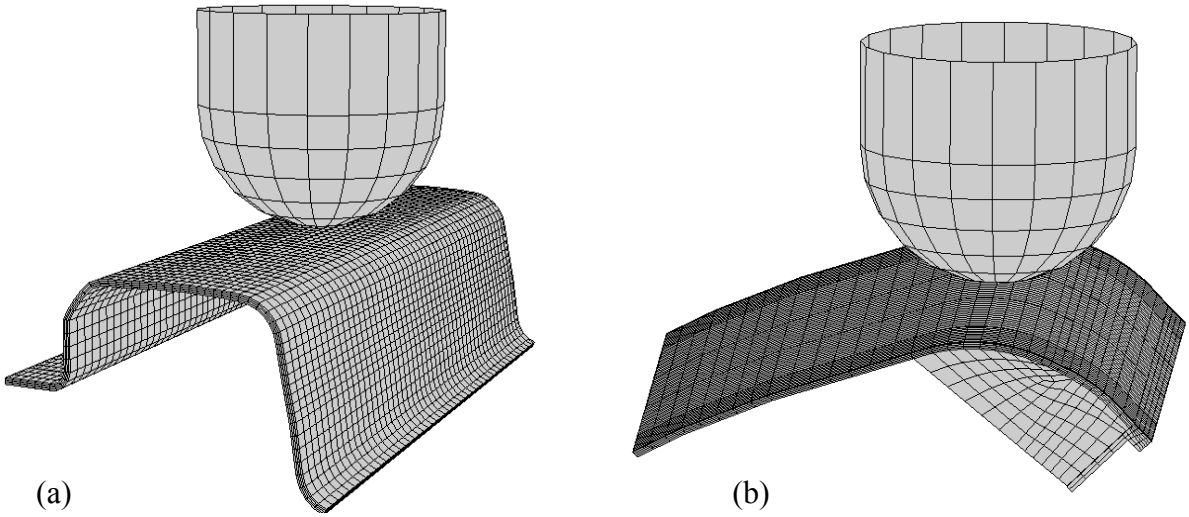

Figure 20. Finite element meshes used for (a) armrest and (b) toptrim components.

6.2 MATERIAL PROPERTIES AND PARAMETERS

The three models investigated were run with a loading speed of 10 mm/s using the parameters in Table 1 for the von Mises (uses E, ν^e and $\sigma_T(\varepsilon_T^p)$ only) and linear Drucker-Prager models and Table 2 for the cavitation model. A full description of the meaning and determination of these parameters are given in sections 3.3 and 3.4 respectively.

In many finite element systems, facilities are available for including the dependence of yield behaviour on strain rate (rate-dependent plasticity) characterised by a series of hardening curves at different strain rates. Whichever elastic-plastic model is used

for a stress analysis, more accurate predictions will be made if the dependence of properties on strain rate is taken into consideration. Rate-dependence must be used to investigate the influence of loading speed. For all models rate-dependent analyses were run. In the case of the von Mises and linear Drucker-Prager models a series of tensile hardening curves, $\sigma_T(\varepsilon_T^p)$, were input. Examples of these curves are given in Figure 10. In the cavitation model effective shear hardening curves $\sigma_o(\varepsilon_o^p)$ are used as the hardening data and the same procedure was used to obtain curves at high strain rates as was used above for the tensile data. Instead of including a series of hardening curves in the input files, mathematical functions given by equations (26) and (27) are used to describe the shape of the hardening curve and its variation with strain rate. Curves at any strain rate can be calculated in an analysis using the parameter values in Table 6.

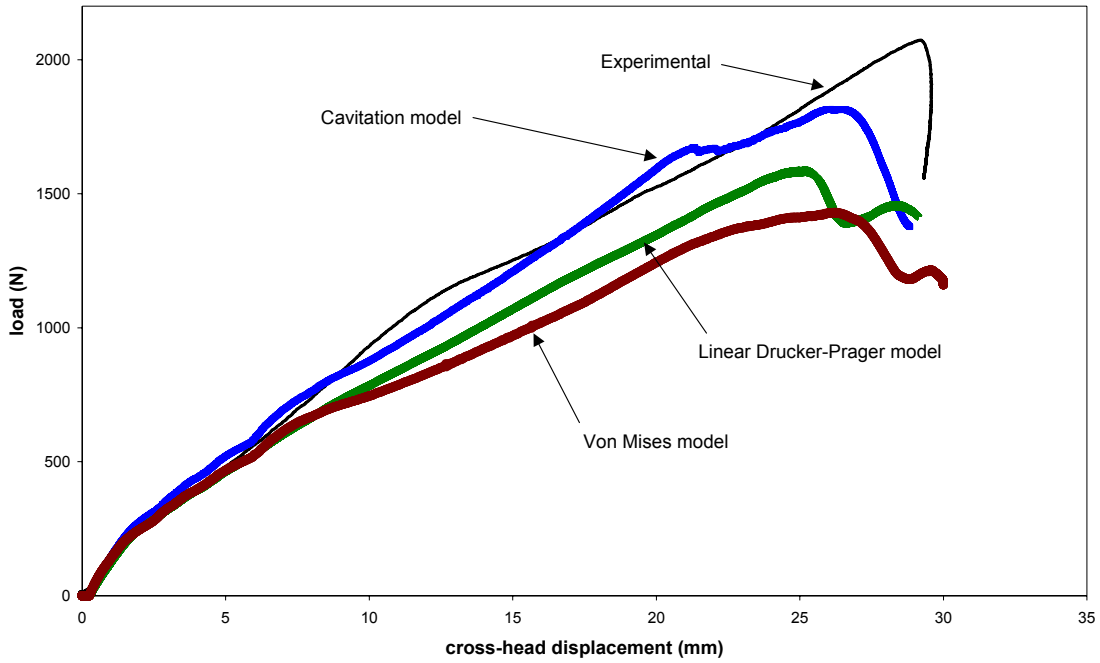

Figure 21. Comparison of measured force-displacement curve for the toptrim component tested at 10 mm/s with curves predicted using the von Mises, Linear Drucker-Prager and cavitation models.

7 COMPARISON OF PREDICTED AND MEASURED BEHAVIOUR

7.1 TOPTRIM COMPONENT

Force-displacement predictions obtained for the toptrim component at a test speed of 10 mm/s using the three models are shown in Figure 21. A typical experimental curve, obtained at the same loading speed, is also shown. It was found that the von Mises prediction was furthest from the experimental data. The linear Drucker-Prager prediction is nearer the test data, and the cavitation model is closer still. This trend demonstrates, as expected, that the more complex models are better at predicting the deformation of the component.

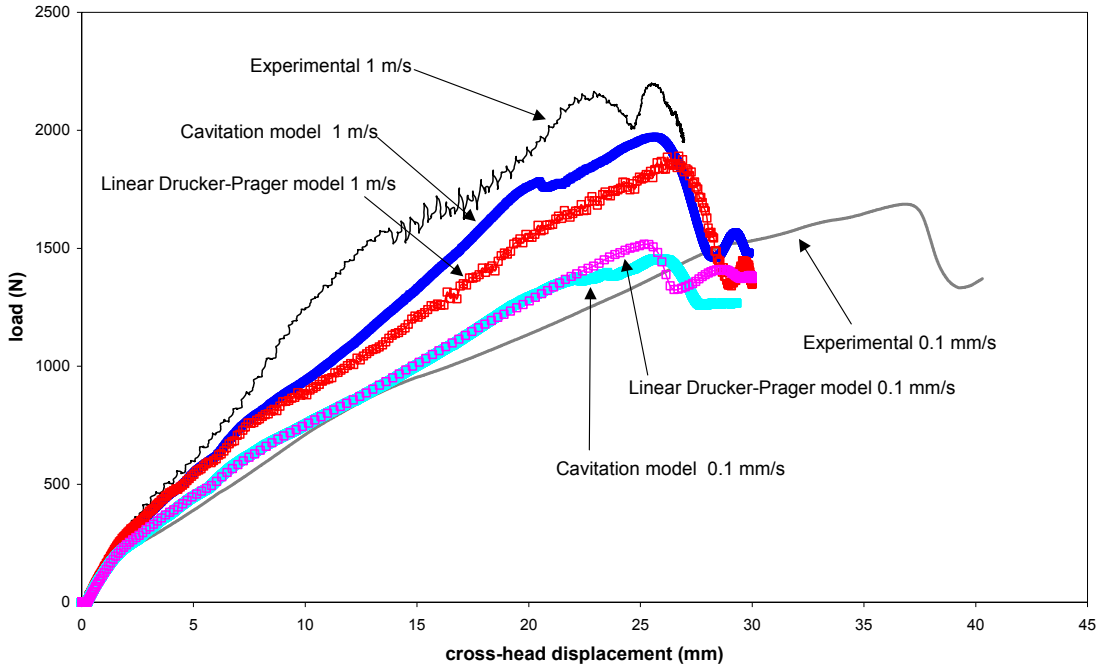

Figure 22. Comparison of measured force-displacement curves for the toptrim component tested at 0.1 mm/s and 1 m/s with curves predicted using the Linear Drucker-Prager and cavitation models.

The component parts were tested at two further speeds, 0.1 mm/s and 1 m/s. Predictions using the linear Drucker-Prager and cavitation models were also obtained at these rates and compared to typical test data, see Figure 22. At 0.1 mm/s the linear Drucker-Prager and cavitation model predictions are very similar and there is a good correlation between the experimental and predicted results, while at 1 m/s the cavitation model provides the closest prediction, although the predicted forces are slightly lower than those measured experimentally. This probably arises because the

value used for tensile modulus is appropriate for low speed tests but, at 1 m/s, a higher value should be used. This is explored in section 8.2.

The photographs obtained during testing have been compared to the deformed plots predicted by the linear Drucker-Prager and cavitation model analyses. Figure 23 shows the photograph of a sample loaded at 0.1 mm/s taken at 20mm displacement with the corresponding deformed plots. The actual component shows deformation of the inner pair of ribs, with no obvious deformation of the outer ribs. This was consistent in all components photographed. The deformed plot predicted by the cavitation model shows the same level of deformation at 20 mm, while the linear Drucker-Prager model predicts that at this displacement the outer ribs would also be deforming. This indicates that the cavitation model is more accurately describing the deformation behaviour of the toptrim component.

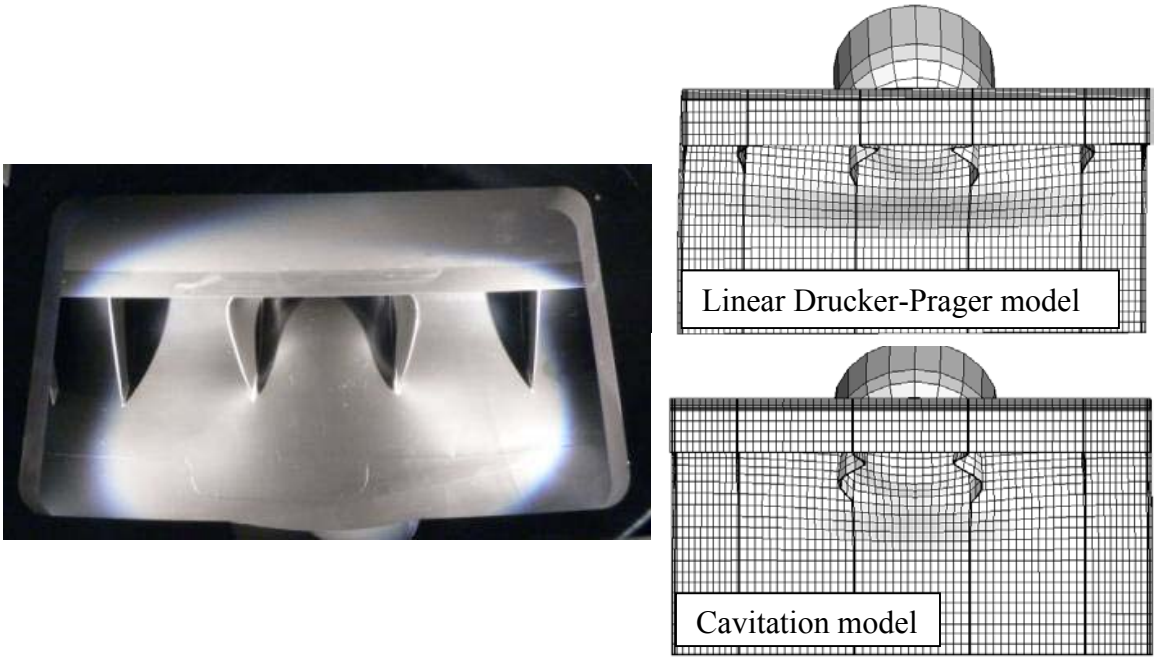

Figure 23. Photograph of the underside of the toptrim component taken at 20 mm displacement. The corresponding deformed plots predicted using the linear Drucker-Prager and cavitation model are also shown.

Predicted maximum principal stress and strain values for the three different models have been studied. In each analysis the values were obtained at the peak load, from the region of the mesh where the indenter contacts the toptrim component. The predicted values are presented in Table 7, and show slight differences between the

linear Drucker-Prager and cavitation models. Stress predictions could be less similar at regions of high strain. The stress predicted by von Mises is slightly higher, and the corresponding strain is much lower than that predicted by the other two models. The stress values predicted are consistent with the peak value in the tensile hardening curves used in the analyses.

Table 7 Maximum Principal Stress and Strain predicted by three elastic-plastic models at the peak load, for the toptrim component

Materials Model	Max Principal Stress (MPa)	Max Principal True Strain
Von Mises	26.8	0.047
Linear Drucker-Prager	23.60	0.076
Cavitation	22.9	0.08

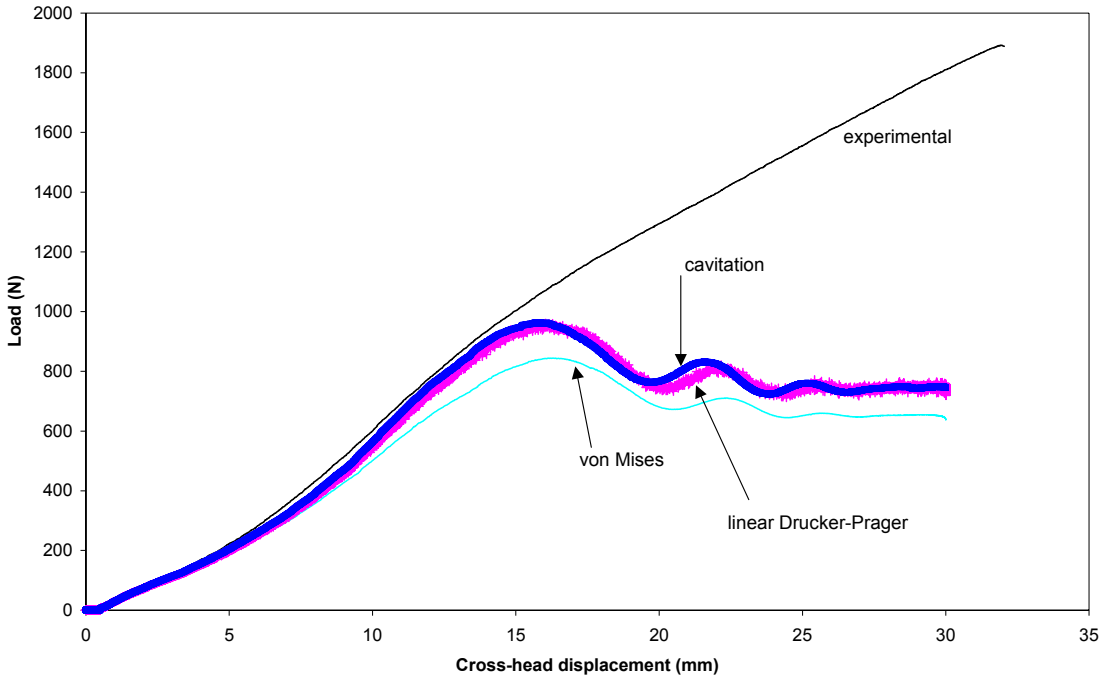

Figure 24. Comparison of measured force-displacement curve for the armrest component tested at 10 mm/s with curves predicted using the von Mises, Linear Drucker-Prager and cavitation models.

7.2 ARMREST COMPONENT

A typical set of experimental data obtained from the armrest component, tested at 10 mm/s is shown in Figure 24. Force-displacement predictions obtained from the three models studied are also plotted. As before, it was found that the von Mises prediction was furthest from the experimental data, with the cavitation model again giving the closest prediction. In all three predictions, the force-displacement curve begins to diverge from the experimental curve at a displacement of approximately 15 mm. The predicted maximum loads are consistently lower than measured loads. Examination of the analyses at a displacement of 15 mm shows that the predicted component shape begins to deviate from that seen experimentally. The predictions show the armrest partially collapsing over to the right side, whereas in reality the armrest stays reasonably upright with the sides deforming outwards (see Figure 25). The reasons for this deviation from experimental data are investigated in section 8.4.

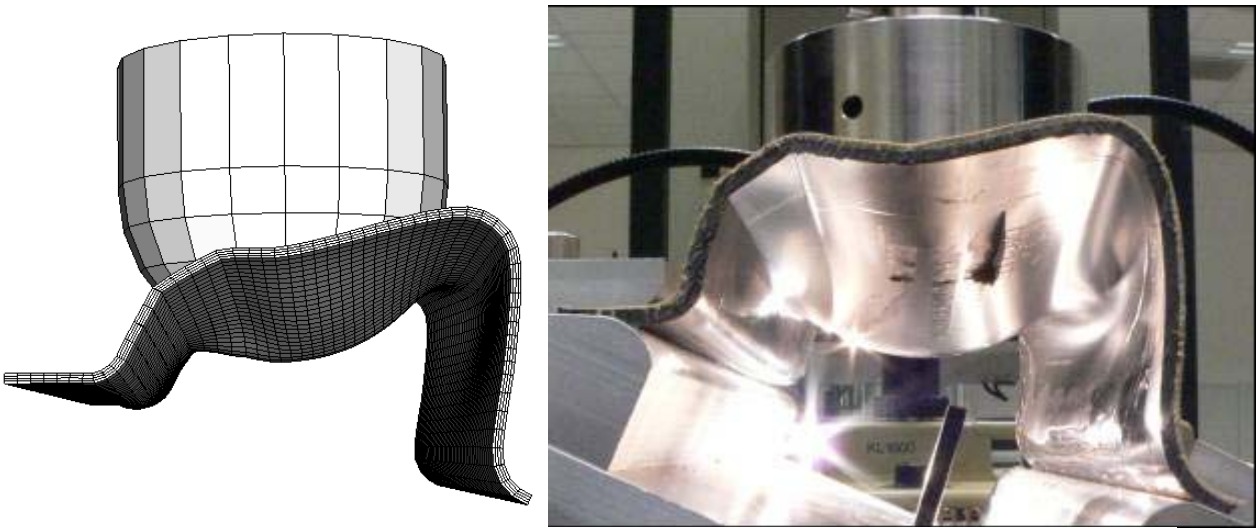

Figure 25. Photograph of the armrest component taken at 20 mm displacement. The corresponding deformed plot predicted by the cavitation model is also shown.

Predicted and measured force/displacement curves obtained for the armrest component at loading speeds of 0.1 mm/s and 1 m/s are compared in Figure 26 using the cavitation and linear Drucker-Prager models. Initially there is very good agreement between the experimental and predicted curve at 0.1 mm/s, with little difference between the predictions from the two models. The correlation at 1 m/s was poorer, although the cavitation model is closer to the experimental data. This is analogous to the toptrim predictions. The predicted force-extension curves show a

deviation from experimental data at an extension of approximately 15 mm, due to the predicted partial collapse of the component.

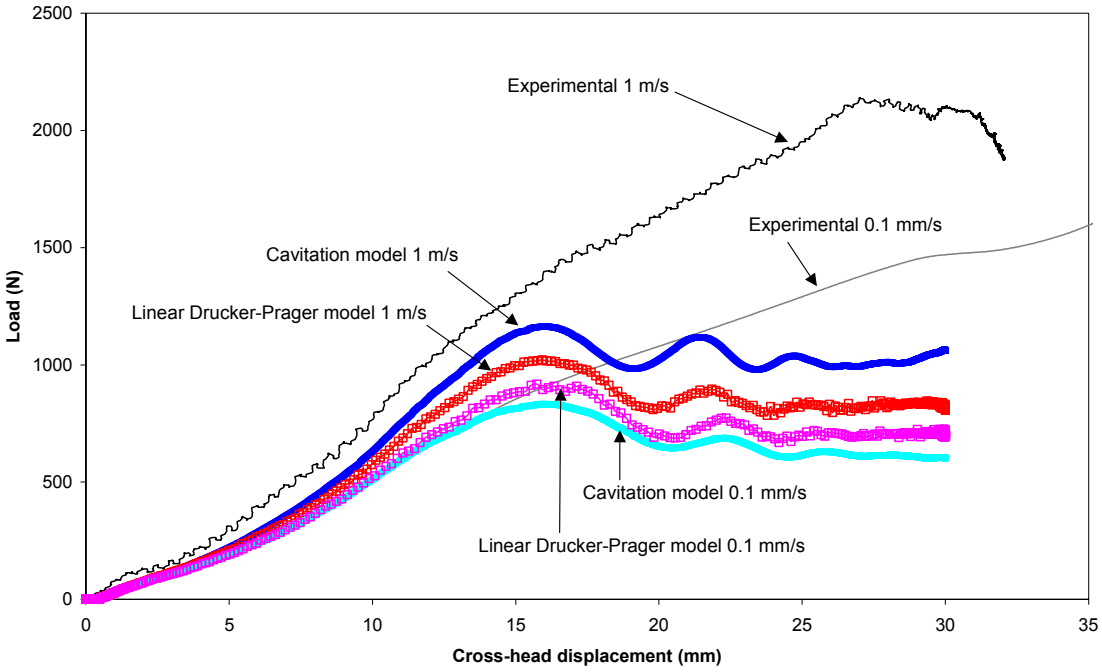

Figure 26. Comparison of measured force-displacement curves for the armrest component tested at 0.1 mm/s and 1 m/s with curves predicted using the Linear Drucker-Prager and cavitation models.

The maximum principal stresses and strains have been studied at the peak loads (approximately 15 mm displacement). Values were obtained from central elements directly underneath the indenter and are presented in Table 8. The stresses and strains are slightly lower than those predicted in the toptrim but the trends are the same, with the cavitation and linear Drucker-Prager models giving similar predictions and the von Mises showing a higher stress but a lower strain.

Table 8 Maximum Principal Stress and Strain predicted by three elastic-plastic models at the peak load, for the armrest component

Materials Model	Max Principal Stress (MPa)	Max Principal True Strain
Von Mises	25.2	0.042
Linear Drucker-Prager	21.6	0.053
Cavitation	21.0	0.051

8 EVALUATION OF THE SENSITIVITY OF PREDICTIONS TO PARAMETERS IN THE FE ANALYSIS

When an FE analysis is set-up initially, user judgement is required on a number of aspects – what element types to use, how fine the mesh is, what material model to use, how accurate the parameters need to be, etc. It is useful to know the sensitivity of results to these types of queries. Once the FE analysis is set-up, it can itself be used to investigate the sensitivity of the system modelled - is indenter location critical, for instance.

Within this work, sensitivity analyses were carried out to study the influence of a range of factors on the deformation behaviour of the two components. The factors included element type, materials parameters, indenter location and specimen alignment and friction.

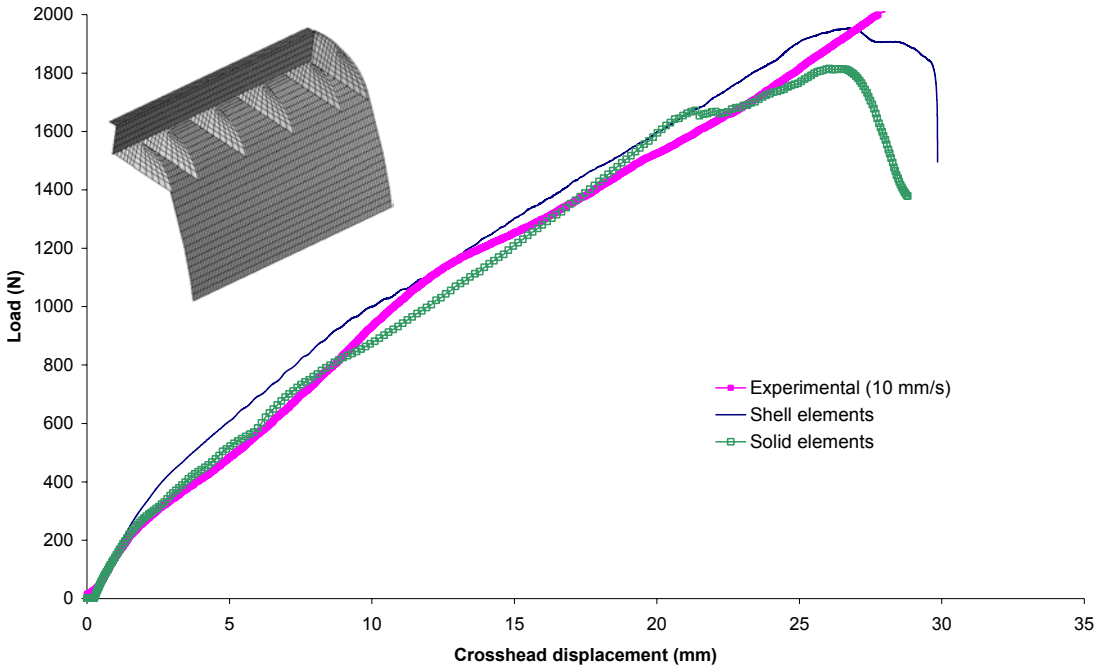

Figure 27. Comparison of the measured force-displacement obtained from the toptrim component at 10 mm/s with predictions obtained from analyses using solid and shell elements.

8.1 ELEMENT TYPE

The initial modelling of the two component parts used solid, continuum elements to give accurate predictions of stress and strain. This was possible due to the relatively small size of the components. In the automotive industry, shell elements are more commonly used due to the computational savings they deliver. To investigate whether shell elements give similar deformation predictions, the toptrim component was remeshed using shell elements and the analysis rerun with the cavitation model, see Figure 27. Although the force-displacement curve obtained using shell elements sits slightly higher than that predicted by the solid elements, they are both giving good predictions of the component behaviour. Comparison of the deformed plots at 20 mm (Figure 28) show the same level of overall deformation i.e. inner ribs are highly deformed while outer ribs have not started to deform. Predicted maximum principal stress and strain values have been studied for both analyses, with values being obtained at the peak load, from the region of the mesh where the indenter contacts the toptrim component. The predicted values are presented in Table 9. The stress values are comparable for both element types, but the strains predicted when using shell elements are less than half those predicted from the solid elements. This suggests that although the shell elements are able to predict the overall deformation of the component well, solid elements perform better in stress and strain analyses.

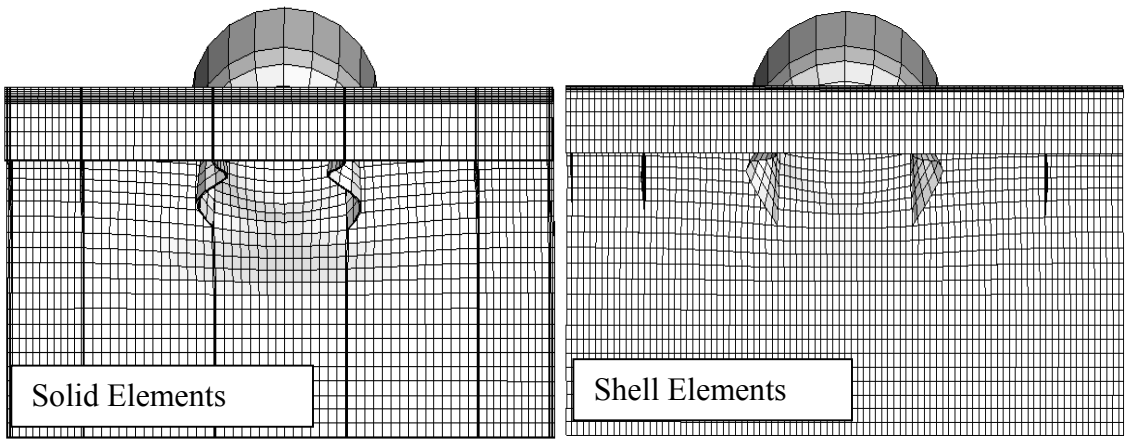

Figure 28. Deformed plots predicted by analysis using the cavitation model with (a) solid elements and (b) shell elements.

Table 9 Maximum Principal Stress and Strain predicted by the cavitation model for the shell and solid element cases at the peak load (toptrim component)

Element Type	Max Principal Stress (MPa)	Max Principal True Strain
Shell elements	23.5	0.033
Solid elements	22.9	0.08

8.2 MATERIAL PARAMETERS

Table 10 demonstrates the number of parameters that are required to use the cavitation model. Some may be assumed to be broadly independent of polymer type (q_1 and μ_1'), while others need to be measured. Some of these measured values are consistent with those used in the linear Drucker-Prager analysis (E, ν^e), while others are unique to the cavitation model. When data are required from tests under two stress states, for example in the calculation of μ, it is likely that the parameter value will depend upon which pair of data points are selected, see section 3.3. Sensitivity analyses have been undertaken to get a feel for the effect of these parameters on the prediction obtained. A full-scale parametric study has not been carried out. Instead the parameters have been individually changed to values that roughly correlate to the uncertainty in the measured value.

One armrest analysis was run at 10 mm/s using a full set of parameters that had been obtained from data at 0.01 s^{-1}, shown in Table 10. Six further analyses were then run, each having a single parameter changed except in the case of the parameters σ_{ofo} and C, which are used to define the effective shear flow stress and its dependence on strain rate (see equation (29)) and were changed together. The new values used for each of these parameters are also shown in Table 10.

Table 10 Values for parameters in the cavitation model at a strain rate of 0.01 s^{-1}

Parameter	0.01 s^{-1} Data	New Values
E (GPa)	1.99	2.45
ν^e	0.37	
μ	0.21	0.3
ν_C	0.47	0.45
k	2.55	
q_1	1.5	1.53
μ_1'	0.17	0.12
ε_{1v}	0.0022	
ε_{2v}	0.01	
β	0.5	
σ_{ofo}	35.9	28.7
C	3.9	3.1

Figure 29 reveals that small changes in the parameters μ, ν_C, q_1 and μ_1' have no significant effect on the predicted force-displacement curves. The parameters σ_{ofo} and C are responsible for the rate-dependence calculations within the model, where σ_{ofo} is the flow stress. Lowering σ_{ofo} and C is seen to significantly reduce the peak load predicted. From this set of analyses it appears that the value used for Young's modulus also has a significant effect on the force-displacement plots. The modulus had been increased to 2.45 GPa (a typical value obtained from data tested at a strain rate of 10 s^{-1}) and this produced a predicted force-displacement curve that was much higher than all the other curves in Figure 29. The low value used for E presumably explains the discrepancy between measured and predicted curves at a speed of 1 m/s observed in Figures 22 and 26. It also indicates that rate-dependent elasticity could have a place in these analyses. Rate-dependent elasticity has been coded into the cavitation model, but has not been fully verified. This is a subject for further work.

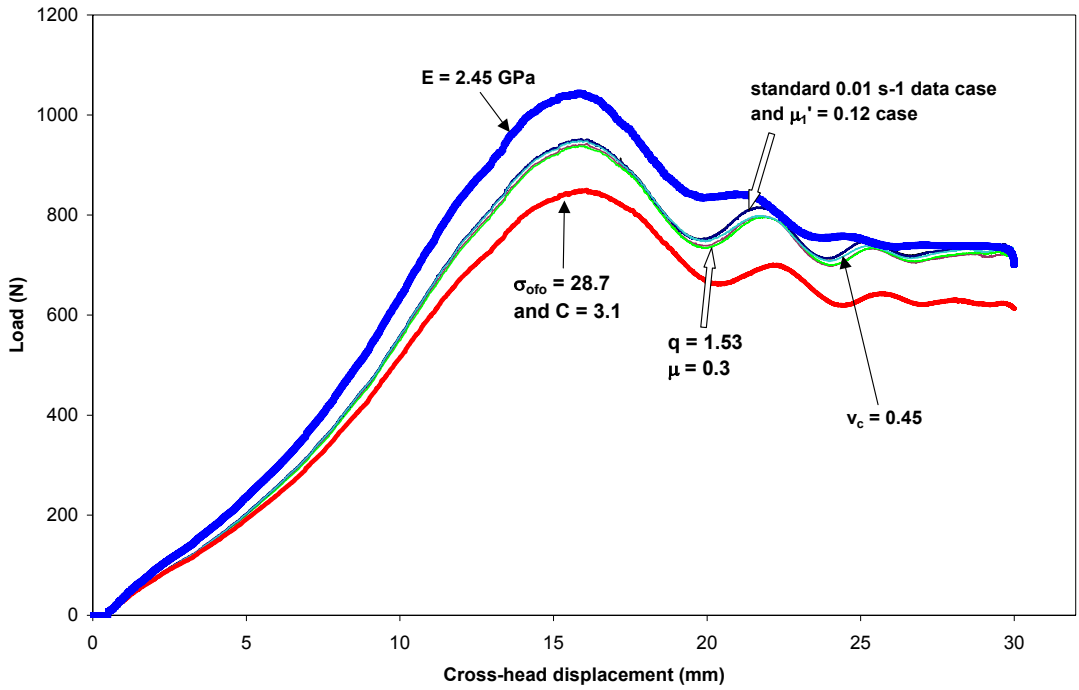

Figure 29. Force-displacement curves predicted using cavitation model as part of sensitivity analyses. One analysis was run with 0.01 s^{-1} data. Subsequent analyses had a single parameter changed.

Table 11 Maximum Principal Stress and Strain predicted by cavitation model with different input parameters, for the armrest component at the peak load

Changed Cavitation Model Parameter	Max Principal Stress (MPa)	Max Principal True Strain
Original 0.01s^{-1} data	21.0	0.051
Increase modulus	21.2	0.054
Decreased rate-dependence parameters	16.3	0.054

The predicted maximum principal stress and strain values were obtained for the two cases that produced significantly different force-displacement curves. Values were obtained from central elements directly underneath the indenter at the peak loads (approximately 15 mm displacement) and are presented in Table 11. The results show that although changing the modulus raises the peak load observed, the actual stresses and strains predicted in the region analysed were very similar to those obtained in analysis using the original 0.01s^{-1} data. In contrast, lowering the rate-dependence

parameters has had a significant effect on the predicted stress, although the strain level remains similar.

It was seen in Figure 29 and Table 11 that changing the rate-dependent behaviour has a large effect on predictions. In some instances FE analysts may only be able to obtain hardening data at a single rate. Rate-independent (single-rate) analyses have been carried out using the linear Drucker-Prager model. Low-rate hardening curves (approximately $0.001s^{-1}$) are the easiest to measure, so a single-rate analysis was run with one of these hardening curves. A second single-rate analysis was carried out using a hardening curve at a strain rate of 0.15 s^{-1} that is close to the mean value for the strain rate in a test at a speed of 10 mm/s. Predictions from these analyses are compared with the force-displacement curve predicted in a rate-dependent analysis in Figure 30. The use of a low-rate curve underestimates the peak loads in the component. When more care is taken in selecting a single rate curve, then reasonable predictions can be obtained. As it is difficult to estimate the varying strain rates within a complex shape during impact loading, it is always prudent to include rate-dependent data if possible.

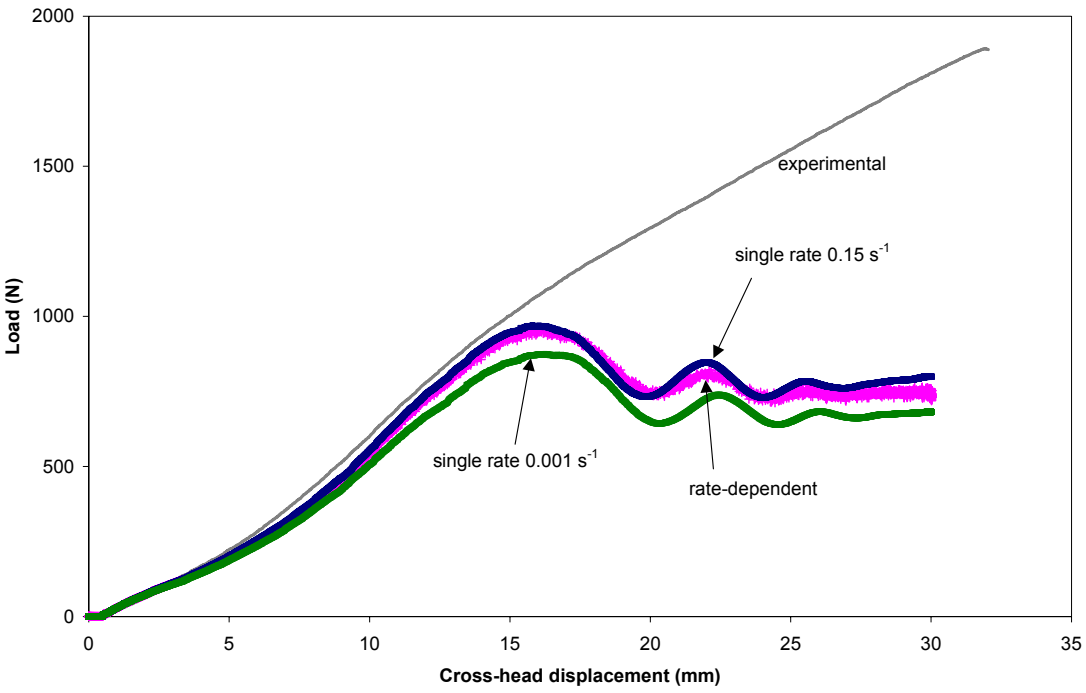

Figure 30. Comparison of single-rate and rate dependent analyses run with the linear Drucker-Prager model at 10 mm/s compared with measured data.

8.3 FRICTION

Armrest FE predictions, presented in Section 7.2, were found to deviate from the experimental data at an extension of 15 mm. This deviation correlated with the predicted partial collapse of the component that was not observed experimentally. One reason for this difference could be due to the lack of friction in the FE models. While friction might keep the indenter central in the laboratory test, the lack of it in the FE model may allow the component surface to slide over the indenter. Therefore friction has been included in an analysis, using a value of 0.2 for the friction coefficient. The inclusion of friction has altered the predicted force-extension plot (Figure 31), as a higher peak load is reached before the load starts dropping off. This leads to an improved correlation with experimental data. The deformed plot included in Figure 31 shows that the armrest component is no longer collapsing to one side, but is staying upright. This matches the experimentally observed deformation.

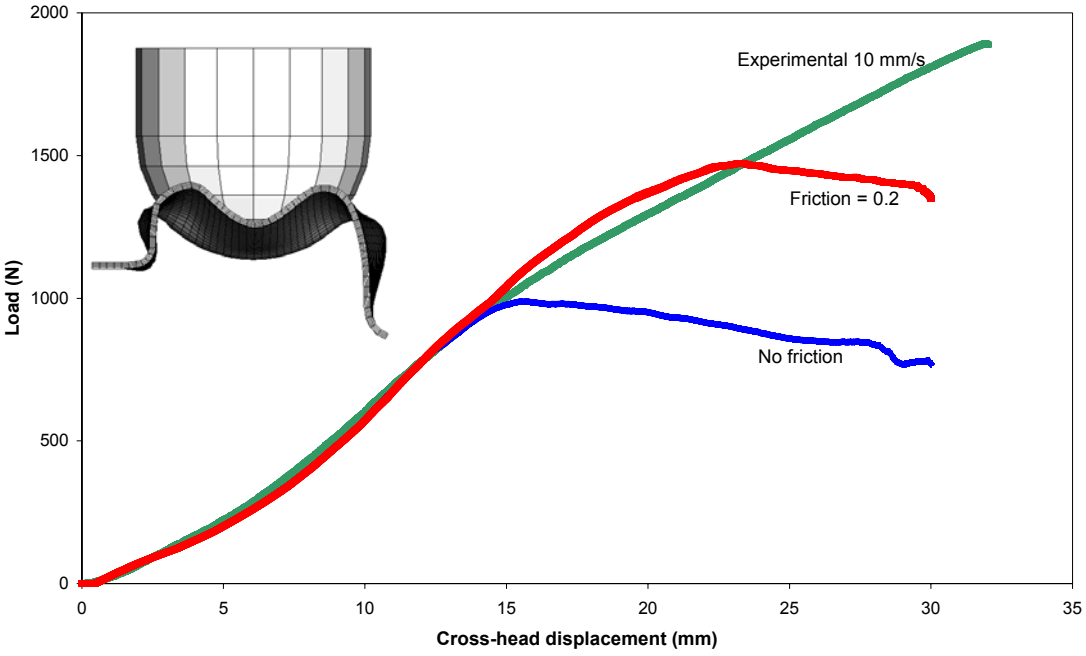

Figure 31. Comparison of armrest predicted force-displacement plots run with and without friction and experimental data at 10 mm/s.

8.4 INDENTER LOCATION AND SPECIMEN ALIGNMENT

Experimental set-up of the component tests includes carefully marking the central point of the loading face to maximise reproducibility between tests, and also to allow direct comparison with FE analyses. During a vehicle collision, passenger impact may occur anywhere along the component parts. FE can be used to investigate how sensitive the deformation of the component part is to impact location. Both components have been studied using the linear Drucker-Prager analysis, with impact occurring at several different locations.

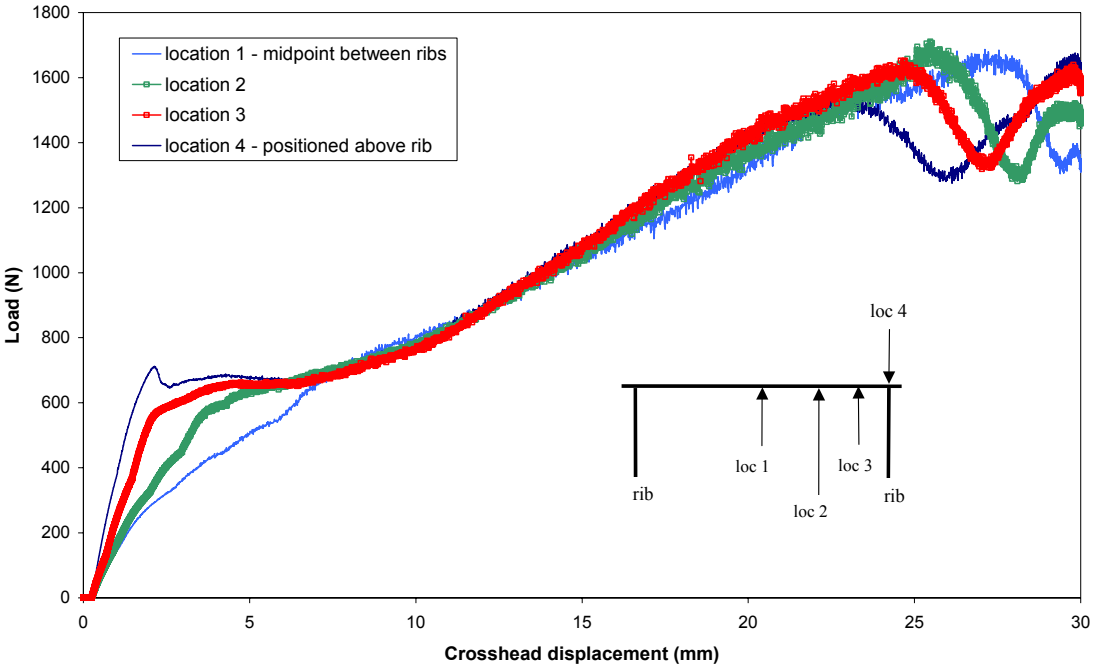

Figure 32. Toptrim force-displacement plots obtained when indenter impacts at 4 different locations.

For the toptrim component the indenter was set to impact at the midpoint between the two central ribs; directly above a rib and at two locations between these two. There is a large difference between the results at small displacements, see Figure 32. The component response is much stiffer when impact occurs above a rib. By a cross-head displacement of 7 mm the four force/displacement curves have coincided. The curves that showed the highest initial stiffness have slightly lower maximum loads.

In the case of the armrest component, five impact locations were chosen; a central position plus 5 mm and 10 mm to the left and right of the centre of the cross-section, see Figure 33. All impacts occurred at the mid-point along the length of the armrest. Impacts occurring 5 mm from the central location had similar shape curves to the central case. Moving the indenter 5 mm to the right increased the maximum load slightly, while moving to the left lowered the maximum load. Moving 10 mm away from the central location caused a large change in the force/displacement plots, with higher stiffness predicted. The two curves were a similar shape to each other although impact on the left hand side had a much lower maximum load.

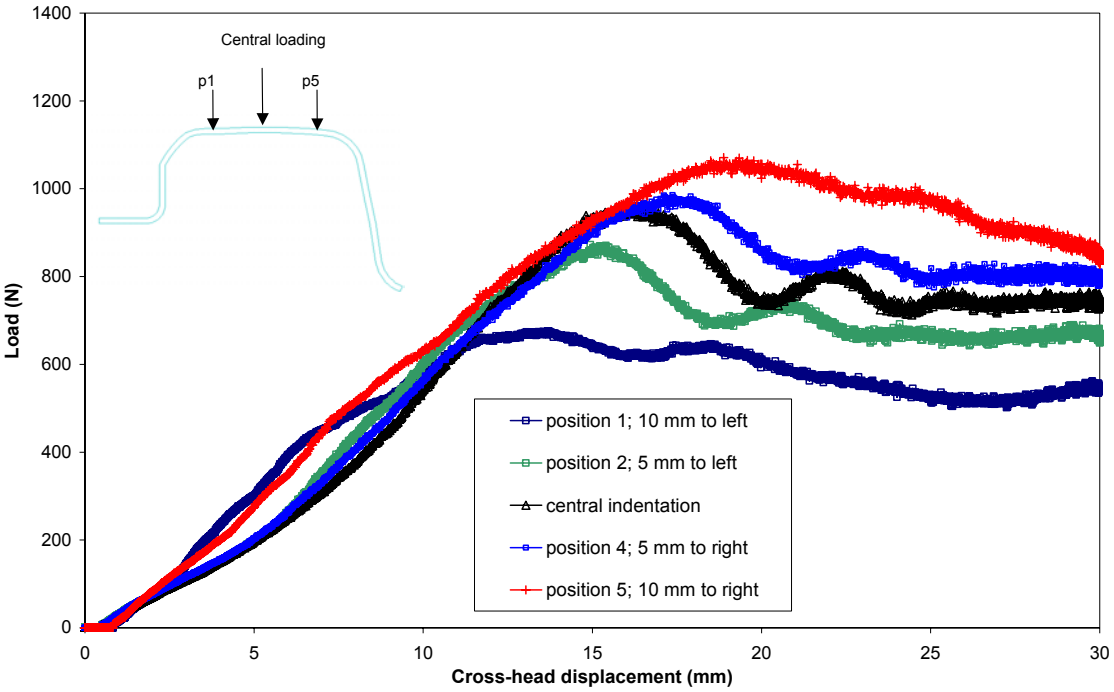

Figure 33. Armrest force-displacement plots predicted when indenter impacts at 5 different locations.

With the armrest clamping jig, specimen alignment is another variable that can be adjusted. Before testing the clamping jig is angled so that the top surface of the armrest is horizontal. This is a potential source of error when looking at the reproducibility between tests. Two FE analyses were run, with the armrest rotated by ±3° to simulate slight misalignments during testing. The results of these analyses (Figure 34) shows only small differences between the predictions indicating that although good alignment is always important for reproducibility in experimental data, exact alignment is not critical.

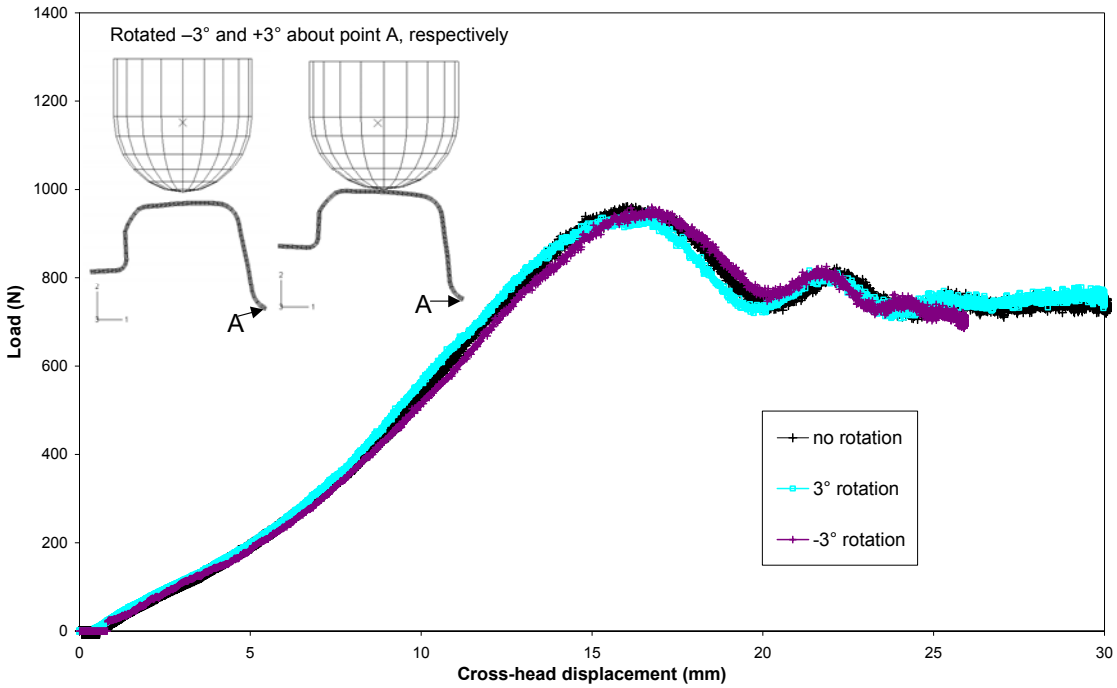

Figure 34. Predicted force-displacement plots obtained when specimen is rotated by ±3°.

9 CONCLUSIONS

Finite element systems use elastic-plastic models to describe the non-linear, large-strain behaviour of rigid materials. Although not developed for plastics materials, these models can be used to simulate the deformation of a component under impact loading. The accuracy of predictions will depend on the suitability of the model for the polymer being studied and the accuracy achieved in the determination of model parameters.

The elastic-plastic model based on the von Mises yield criterion is the simplest model but neglects any influence of the hydrostatic component of stress on yield behaviour. The data requirements for this model can be derived from tensile tests alone. The linear Drucker-Prager model is more accurate for plastics than the von Mises model since it accounts for some influence of the hydrostatic component of stress on yield behaviour. Determination of the additional parameters for this model requires data from tests in tension and one other stress state such as shear or compression. Hardening behaviour for these models can be characterised by a stress vs plastic strain curve in tension. The measurement of this curve cannot be achieved accurately using

standard tensile specimens and requires the use on a novel specimen geometry. The yield behaviour of plastics depends on strain rate so, for maximum accuracy in predictions, hardening curves should be determined over a range of strain rates relevant to the application. These properties can be determined from measurements of tensile hardening curves at low and moderate strain rates and deriving curves at higher strain rates by modelling and extrapolation.

Using these models, it is not possible to accurately predict stress/strain behaviour under shear and compression and the strain dependence of Poisson's ratio for materials that exhibit significant cavitation (void formation) under tensile stress states. The cavitation model takes account of the nucleation of cavities on yield behaviour under stress states where there is a hydrostatic component sufficient to nucleate the cavities. Cavities nucleate in the more mobile regions of the polymer, which in the material studied here are presumably the amorphous phase and the rubber toughening particles. Debonding at the interface with filler particles may also contribute to the overall effective volume fraction of voids. The nucleation of cavities is assumed to be determined by the level of volumetric strain and to take place over a range of volumetric strain for a distribution in the size of the mobile regions. The hardening behaviour in this model is characterised by a curve of the effective shear stress against effective shear plastic strain. Hardening behaviour at high strain rates can be determined in the same way that has been described for tensile properties.

Measurements of flow stresses in tension and shear over a range of strain rate indicate that the volume fraction of cavities in a propylene copolymer when cavitation is complete increases with increasing rate. This is supported by measurements of Poisson's ratio with strain at different strain rates.

The use of finite element analysis to predict the deformation behaviour of two plastic components has been investigated. When compared to the cavitation model, the linear Drucker-Prager was found, for the cases investigated, to be adequate despite the simplifying assumptions, although stress and strain predictions may be dissimilar at regions of high strain. The von Mises model gave the least accurate predictions of component behaviour. In this study modulus and flow stress (σ_{ofo}) were found to be

the most influential materials parameters in the cavitation model. In the small region of elements studied, changing modulus had little effect on predicted stress and strain values, while changing the flow stress caused a significant change in predicted stress.

Rate-dependent plasticity should be included when predicting deformation behaviour over a range of loading speeds to give more accurate predictions. Friction occurs between the component surface and the indenter and so should also be included in the analyses. It was found that shell elements are able to predict the deformation of the component accurately. The strain predictions obtained with shell elements are not as robust as those obtained using solid elements.

10 ACKNOWLEDGEMENTS

The authors acknowledge the contribution to this work by F. Dunne at Oxford University with writing the code to enable the cavitation model to be used with the ABAQUS finite element system. The assistance is also acknowledged of L. Wright at NPL with the application of the cavitation model in ABAQUS, of R. Mera at NPL with the measurement of material properties and of N. Lourenco and R. Brown at Jaguar Land Rover with the supply of door trim mouldings. The work was funded by the Department of Trade and Industry as part of the Measurements for Processing and Performance programme.

11 REFERENCES

1. C. B. Bucknall: in ' The Physics of Glassy Polymers', ed. by R. N. Haward and R. J. Young, 2nd edn., ch.8, 1997, Chapman and Hall.
2. A. Lazzeri and C. Bucknall. J. Mat. Sci., (1993), **28**, p 6799.
3. B. Read and G. Dean. Plastics, Rubber and Composites, (2001), **30**, p 328.
4. I. M. Ward: in 'Mechanical Properties of Solid Polymers', 2nd edn, ch.11, 1983, John Wiley and Sons, Ltd.
5. R. Raghava, R. M. Caddell and G. S. Yeh: J. Mater. Sci., 1973, **8**, 225.
6. A. Gurson. J. Eng. Mater. Technol., Trans ASME, (1977), **99**, p 2.
7. V, Tvergaard. Int. J. Fract. Mech., (1981), **17**, p 389.
8. C.B. Bucknall, A. Karpodinis and X. Zhang. J. Mat. Sci., (1994), **29**, p 3377.

9. G. Dean, B. Read and L. Wright. NPL Report MATC(A)120, September 2002
10. G. Dean and L Crocker, NPL Good Practice Guide No. 87, 2006
11. ISO 527-2, Plastics – Determination of tensile properties – Part 2: Test conditions for moulding and extrusion plastics.
12. G. Dean and B. Read. Polymer Testing, (2001), **20**, p 677